DETERMINATION OF ENDOSPERM PROTEIN SECONDARY STRUCTURE IN HARD WHEAT BREEDING LINES USING SYNCHROTRON INFRARED MICROSPECTROSCOPY AND REVELATION OF SECONDARY STRUCTURAL CHANGES IN PROTEIN FILMS WITH THERMAL PROCESSING

by

EMILY SUSANNE BONWELL

B.S., University of Illinois, 2005

A THESIS

submitted in partial fulfillment of the requirements for the degree

MASTER OF SCIENCE

Department of Grain Science and Industry
College of Agriculture

KANSAS STATE UNIVERSITY
Manhattan, Kansas

2008

Approved by:

Major Professor
David L. Wetzel

Abstract

Fourier transform infrared microspectroscopy was used to determine protein secondary structure in hard wheat breeding lines *in situ*, providing a molecular means to rank endosperm hardness for the selection of wheat cultivars for a specific end-use. Mapping with a single masked spot size diameter of 4.5 μm or confocal 5 μm on beamlines U10B and U2B, respectively, produced spectra from the subaleurone layer within each wheat kernel using the high spatial resolution available with synchrotron infrared microspectroscopy. This procedure was used for the first four crop years. A focal plane array instrument was adapted for use for the remaining two crop years with a slight reduction of spatial resolution. Deconvolution and curve fitting were applied to the amide I region of spectra selected from the interstitial protein between the starch granules, and the relative amount of α-helix to other protein secondary structures was revealed. Over six crop years, the α-helix to β-sheet ratio of experimental wheat varieties were compared to those of released varieties in 143 mapping experiments. The highest measurable value was 2.50 while the lowest was 1.11, a range consistent with hard wheat secondary structure determination found in previous studies **(13, 16)**. The determination of protein secondary structure provides a means of ranking experimental breeding lines for selection in specific end-use applications.

FT-IR microspectroscopic imaging was used to develop a method, using myoglobin as the model protein, to study the effects of thermal processing to 100 ˚C on protein secondary structure. Films cast onto highly polished stainless steel plates allowed the study of the exact same film before and after heating. Analyzing the shift in the amide I peak maxima of reflection absorption spectra for 280 pixels from myoglobin films revealed the depletion of α-helix at the expense of other protein secondary structures. Deconvolution and curve fitting techniques were applied to the amide I region of each spectral average to model protein secondary structure components found within the region. The method developed was applied to another animal source, gelatin, and a plant source, wheat gluten.

Table of Contents

List of Figures

List of Tables

Acknowledgements

First, I would like to thank my love, Clay Karz, for all of his emotional support and love during my graduate career. I would also like to thank my father, Keith Bonwell, mother, Peggy Tingley, and sister, Jessica Bonwell, for their love and support not only through my graduate career, but also throughout my entire life.

A special thanks goes to my advisor, Professor David Wetzel, whose recruitment and guidance encouraged me to attend Kansas State University. Thank you to Professor Paul Seib and Professor Chris Culbertson, my committee members, for the knowledge imparted from courses taken under their supervision and for serving as committee members.

Finally, I would like to thank my labmates and friends for their support, love, and laughs throughout my college career.

Chapter 1- Determination of Endosperm Protein Secondary Structure in Hard Wheat Breeding Lines Using Synchrotron Infrared Microspectroscopy: Ranking endosperm hardness based on the ratio of alpha helix to beta sheet.

Literature Review

Cultivars exclusively in the hard wheat class vary in their potential as bread quality wheat lines. The same molecular structural features that clearly differentiate the endosperm of hard from soft classes are a convenient objective means to facilitate hardness trait ranking among breeding lines. The hardness of wheat endosperm remains the single most important trait in selecting wheat to produce flour for specific end-uses. Three classes of wheat increasing in hardness are soft, hard and durum. Applications of soft wheat flour include cake and pastry making, while durum is used exclusively used for pasta manufacturing. Flour produced from the endosperm of wheat belonging to the hard wheat class is known to be the most desirable for bread making and is the main focus of this study. Determining the hardness level of wheat endosperm not only allows bakers to specify a desired quality, but also breeders to select an experimental variety that will be used for future breeding lines and scientists to research specific attributes related to cereal quality. Physical methods have been used to define wheat kernel hardness and its resistance to deformation. Soft wheat endosperm is characterized by the tendency to fracture more easily, providing low levels of starch damage and the production of flour of fine particle size. Hard wheat, on the other hand, tends to have fracture planes, high levels of starch damage and coarser particle size. Within the past two decades, with the broadening of the genetic base of wheat, new breeding lines have required sophisticated instrumentation to carefully monitor endosperm hardness. The objective of this study is to apply a molecular based approach to endosperm hardness that, until recently, has not been practical.

Wheat Endosperm Hardness

Genetic Consideration: It wasn't until the 1960s that hardness was not a mere factor of physical resistance, but a matter of the structure of endosperm protein. Symes postulated in the

mid 1960's that through particle size index measurements and backcrossing of hard and soft wheat breeding lines, that hardness was a result of gene expression **(1)**. In 1973 it was suggested that hardness was related to the adhesion of protein to the starch molecule and the molecular weight of this protein **(2, 3)**. In that same year, the gene controlling grain hardness, *Ha*, was found to be located on the short arm of 5D chromosome **(4)**. The *Ha* gene is linked to the production of Friabilin, a 15 kDa polypeptide also known as the Grain Softness Protein, GSP, and is found on the starch granule surface of soft wheat varieties but absent or only slightly expressed in durum and hard wheat, respectively **(5)**. Friabilin is further composed of 2 proteins, puroindoline-a and -b. These are found in the starchy endosperm and thought to bind lipids through the tryptophatic rich regions from which they were named **(6)**. This could be related to the lack of adhesion between the starch granules within soft wheat endosperm. It was further shown that a mutation on the 46^{th} position of puro-b, causing a change from a glycine amino acid residue to serine in hard wheat changes the protein structure, thus decreasing the affinity for membrane lipids **(7)**. In addition, it was found that other mutations can cause wheat endosperm hardness. For example, the absence of puro-a, a switch from Leu-60 to Pro-60 or Try-44 to Arg-44 in puro-b, or the absence of puro-b combined with the mutation of Trp-39, Trp-44, or Cys-56 to a stop codon on puro-a. This is summarized in the 2002 review of strictly puroindolines by Morris **(8)**. Turnbull and Rahman **(9)** and Anjum and Walker **(10)** give a complete review of the classification of wheat endosperm texture and the roles of protein and starch thoroughly defining previous work done in the area of endosperm hardness.

Protein Secondary Structure: The PhD dissertation research of Oliver Piot under the direction of Professor Manfeit at the University of Reims, France opened the door and provided motivation for the present study. In the late 90s Piot spoke at the American Association of Cereal Chemists (AACC) conference in Seattle, WA regarding what he termed the millability of wheat. His objective was highly localized chemical analysis of the inner aleurone cell wall in contact with the endosperm. Using confocal Raman microspectroscopy, with the incident laser focused down to a 1 μm spot size, the high spatial resolution achieved enabled the *in situ* study of individual cell walls within the wheat kernel. The concentration and location of ferulic acid, protein and arabinoxylans were related to adhesion and thus the millability (edge of physical separation) of wheat **(11)**. In the subsequent report, changes in ferulic acid derivatives and arabinoxylans in the aleurone cell walls and starchy endosperm during maturation of both hard

and soft wheat varieties, which he again related to physical separation in milling **(12)**. Confocal Raman microspectroscopy was advantageous due to its ability to use samples approximately 50 μm thick. Thick samples allowed the study of wheat kernels throughout the maturation process since immature kernels are essentially impossible to section. Protein secondary structure was determined at four stages of maturation. **Figure 1.1** shows that during the maturation process of hard wheat, the α-helical content increases at the expense of the β-sheet form. In contrast, mature soft wheat had nearly equal amounts of the two forms **(13)**. Point for point spectra from confocal Raman microspectroscopy had excellent spatial resolution for the fundamental French study. Published accounts, by Piot, of other changes involved during maturation, including the cohesion of starch and protein as well as the phenolic compounds and arabinoxylan character through analysis of endosperm cell walls, can also be found **(13, 14, 15)**.

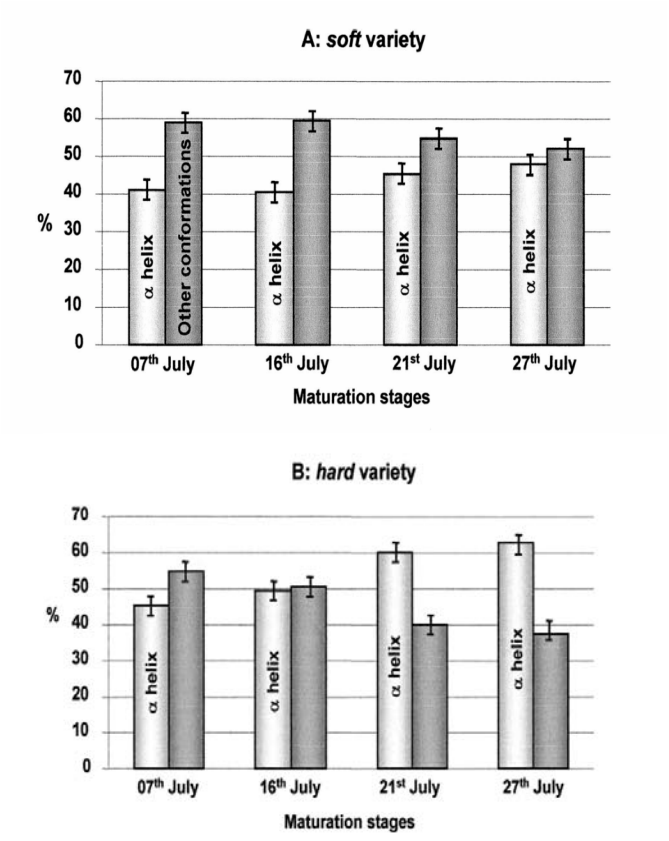

Figure 1.1: Changes in the percentages of α-helix and β-sheet secondary structure in maturing hard and soft wheat varieties. **(Reprinted from 13)**

For assisting Kansas Agricultural Experiment Station wheat breeders mapping with FT-IR microspectroscopy would enable collecting many spectra within the endosperm to use for characterizing alpha-beta ratios of current hard wheat breeding lines. A synchrotron source was used to enhance spatial resolution. The long term study reported here was initiated by Wetzel and coworkers **(16)** who used synchrotron infrared microspectroscopy to determine the relative α-helix to β-sheet ratio in wheat endosperm. Using deconvolution and curve fitting techniques, it was found in the previous study that results corresponded to those with Raman. The range of protein secondary structure ratios for hard wheat was 2.10-1.57, while the range for soft wheat tested 1.07-0.96, see **Figure 1.2**. These results are similar to those seen for mature kernels in **Figure 1.1**. FT-IR microspectroscopy was restricted to the study of mature kernels due to the necessity for 4-6 μm thicknesses.

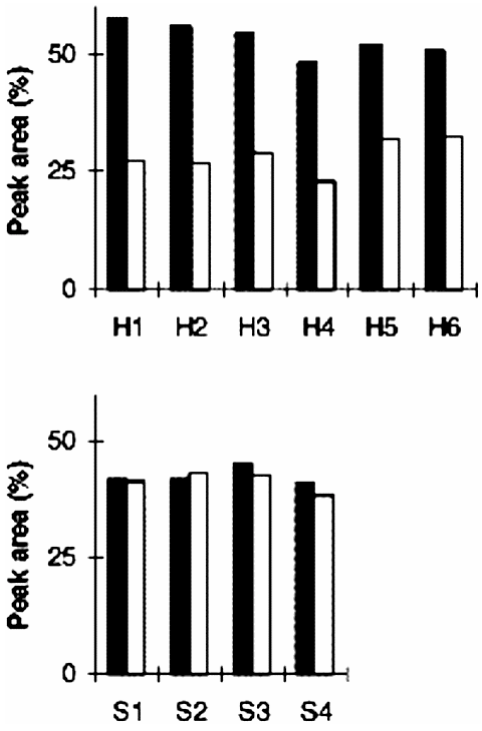

Figure 1.2: Comparison between α-helix (solid) to β-sheet (open) in hard (top) and soft (bottom) wheat breeding lines at maturity. **(Reprinted from 16)**

Molecular Endosperm Hardness Measurements

Protein Structure: The primary structure of proteins consists of a mixed polypeptide chain of any of 20 different amino acids linked together. They differ in amino acid composition

and sequence. A typical amino acid contains the central α-Carbon (C_α) connected to a carboxylic acid group (COOH) and an amine group (NH_2). A third branch exists between the C_α covalently bound to one of the 20 different amino acid side chains. These side chains range from non-polar to polar with positive, negative, or no charge. The amine group of one amino acid forms a covalent bond with the carboxyl group on a neighboring amino acid to form the peptide group shown in **Figure 1.3**.

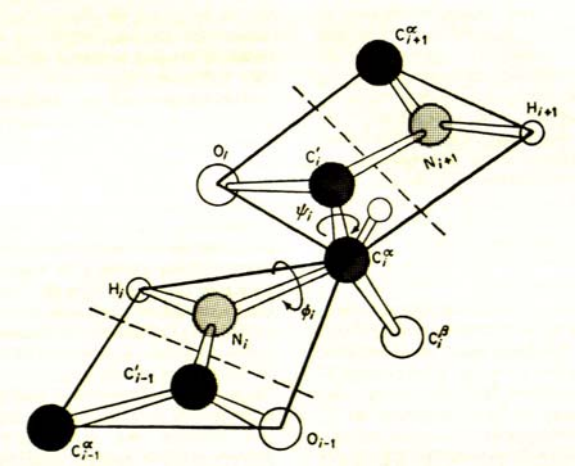

Figure 1.3: Molecular model a typical peptide bond, showing the phi (Φ) and psi (Ψ) angles involved in the rotation of the peptide chain to produce a characteristic secondary structure. **(Reprinted from 17)**

Protein secondary structure has been defined as "the local spatial arrangement of a polypeptide's backbone atoms without regard to the conformations of its side chains" **(18)**. Secondary structure is the shape unto which a protein assembles, governed by the rotation of phi (Φ) and psi (Ψ) angles. Phi is the angle between the α-carbon and nitrogen, and psi is the angle between the α-carbon and carboxyl carbon. Due to van der Waal's forces, phi and psi angles are only able to move to a certain degree. The Ramachandron diagram has widely been accepted as an outline of the allowed conformation of these polypeptides **(18, 19)**. **Figure 1.3** shows the molecules involved in a peptide bond and the location of the phi (Φ) and psi (Ψ) angles.

Alpha helix, **Figure 1.4,** and β-sheet, **Figure 1.5,** are termed "regular secondary structures" due to the repetition of phi and psi angle orientation along the entire length of the structure. The α-helix consists of 3.6 residues per turn with a pitch of 5.4 Å **(18, 19)**. The phi angle is set at -60˚ and psi is -50˚ **(20)**. The oxygen of the nth carboxylic group hydrogen bonds to the n+4 hydrogen of the amine group.

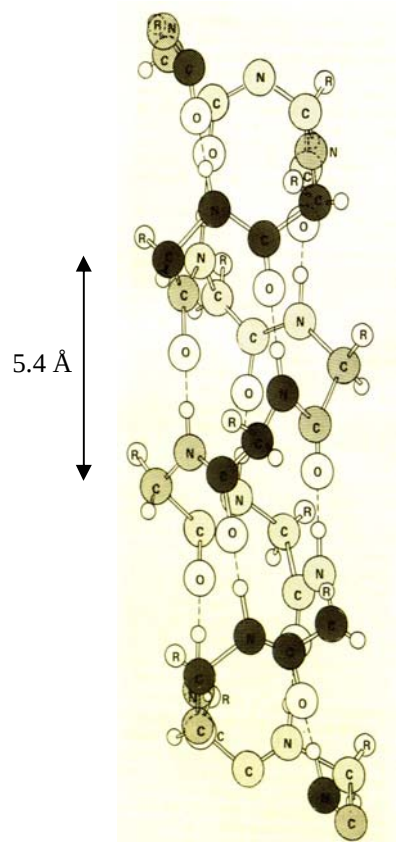

Figure 1.4: Molecular model of a typical α-helix. **(Adapted from 17)**

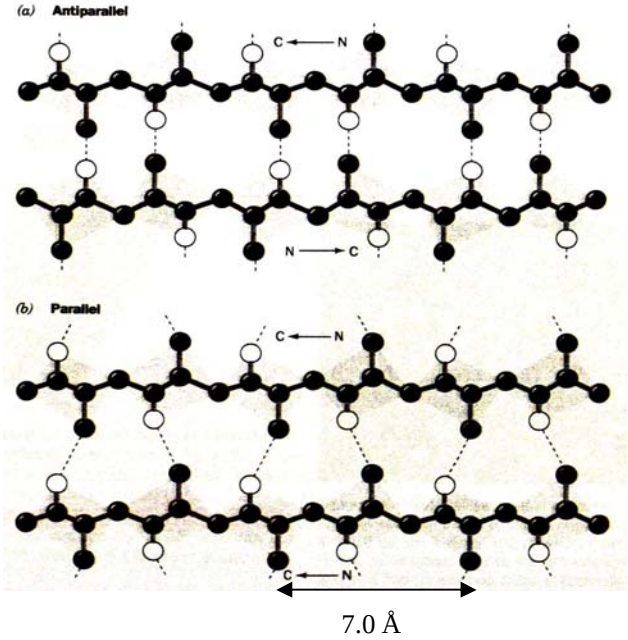

Figure 1.5: Molecular model of an antiparallel (a) and parallel (b) β-sheet. Dashed lines between peptide chains represent hydrogen bonds. **(Adapted from 18)**

Beta sheet, on the other hand, is a combination of hydrogen bonded chains folding into an accordion like shape. Two to 22 chains make up a single β-sheet structure with a pitch of 7.0 Å between each successive accordion fold. The set angles for the β-sheet structure are as follows: $\Phi = -120^{\circ}$ and $\Psi = +140^{\circ}$ **(20)**.

Information regarding other, nonrepetitive, protein structures such as the random coil and β-turn can also be found **(18)**. These structures will be mentioned, but the focus of the present study is α-helix and β-sheet.

X-Ray Diffraction: The connection of electron density, found within a crystalline structure to protein structure is X-ray diffraction. Its application for use in protein structure analysis stems from the work on horse hemoglobin and sperm-whale myoglobin by Perutz **(21, 22)** and Kendrew **(23)**. Now a frequent use of the synchrotron source is diffraction of large proteins. Synchrotron X-ray diffraction has revolutionized the field of protein structural data. The high energy produced by the synchrotron provides extra sensitivity and there is no limit to the protein's molecular weight. X-ray diffraction is an excellent method for determination of three-dimensional structure, but there are, however, associated disadvantages. The most serious is that the protein has to be crystallized and the crystal needs to be of high purity. X-ray instruments are much higher is cost compared to other methods of protein structure analysis **(24)**. Protein extraction is required for crystallization, therefore the *in situ* study of food particles is restricted. Also, the ability to analyze the dynamic characteristics of the protein is impossible.

Vibrational Spectroscopy: Vibrational spectroscopy elucidates molecular structure with fundamental vibrations, ie. infrared and Raman. The mid-infrared region, spanning from 4000-500 cm^{-1} or 2.5-20 μm, is used to study fundamental vibrations involving the vibrational motion of a molecule. A molecule must produce a change in dipole moment in order to exhibit fundamental vibrations. In the condensed phase, stretching and bending vibrations are of interest **(25)**. Infrared spectroscopy has been used to predict protein structure since approximately 1950 through the comparison of X-ray crystallographic data to the amide I band of polarized infrared spectra **(26)**. Elliot and Ambrose were the first to correlate the secondary structure to the amide I region in the infrared spectrum. C=O stretching vibrations are the main contributors to the amide I region spanning from approximately 1700-1610 cm^{-1}. Hydrogen bonding **(24)** and transition dipole coupling (TDC) **(27, 28, 29, 30)** are two theories that have been proposed to relate the frequency of curves within the amide I region to specific secondary structures.

Hydrogen bonding within the α-helix structure, as previously stated, is the non-covalent bond between the oxygen attached to the carbonyl (n) and the hydrogen on the n+4 residue. Jackson and Mantch **(24)** state that the frequency position of a particular peak is related to the strength, length and direction of the hydrogen bond. A hydrogen bond between two turns stabilizea an α-helix, for example, while the β-sheet is stabilized by hydrogen bonding between 2 adjacent strands. The hydrogen bonds between the β-sheet strands are shorter and therefore show up at a lower frequency.

In an extended review of protein vibrations involved in infrared analysis, Barth and Zscherp **(27)** attribute the location of secondary structure frequencies to TDC of neighboring amide bonds. Oscillations across the amide group create waves that constructively or deconstructively interfere. For β-sheet there are two different combinations of constructively interfering waves, and thus the reason for the two β-sheet peaks found within the amide I infrared region. Abe and Krimm studied the effects of TDC on polyglycine **(28)**. Miyazawa used a set of equations referred to as a perturbation treatment in order to characterize vibrations involved between adjacent peptide groups. These vibrations are then related to the frequency of secondary structures **(29).** Work by Mayazawa and Krimm are just a few of the studies that determine protein structure through the force field surrounding the protein. An extended review by Krimm and Bandekar **(30)** of this concept as well as other research on the forces around the peptide bond can be referred to for more information on this theory.

Studies looking at the contribution of amino acid side chains have shown through analysis of protein in solution, that amino acid side chains do, in fact, contribute and add to the amide I absorption. Amino acids such as tyrosine, asparagine, glutamine, arginine, and lysine show minor absorption in the amide I band **(31, 32)**. Reviews have stated that although these could affect the results, attempts to subtract out the spectrum of particular amino acids could introduce artifacts into data analysis **(24, 27)**.

Modern IR microspectrometers are possible when interferometer instruments are used. Fourier transform instruments offer several advantages over the outdated dispersive instruments. The ability to simultaneously record all wavelengths is known as Fellgetts or multiplex advantage. Entrance and exit slits are no longer used to limit the light throughput, thus enhancing the signal (Jacquinot advantage). The use of the liquid nitrogen cooled Mercury Cadmium Telluride (MCT) detector increases sensitivity of the instrument **(33)**.

Fourier transform infrared spectroscopy (FTIR), **Figure 1.6**, involves the introduction of radiant energy into the system. The light hits a beam splitter which, as its name applies, splits the beam into two perpendicular beams. These reflect off of a set of mirrors. One of the mirrors is fixed, while the other moves. The velocity of the movable mirror is related to frequency in the infrared spectrum using the following equation:

$$f = (2/\lambda)*v$$

The reflected energy is recombined by the beam splitter to give constructive interference between the two waves. The detector, typically a liquid nitrogen cooled MCT, acts as a semiconductor when radiation hits, thus producing an electric charge. This charged response is recorded as an interferogram which is then Fourier transformed into the spectrum that one will see **(25)**.

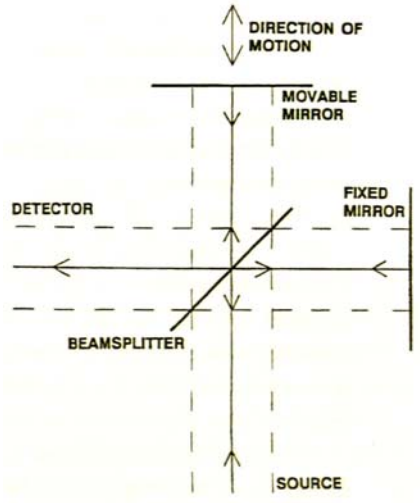

Figure 1.6: Diagram of a typical interferometer. The velocity of the moving mirror is proportional to the frequency of the energy. **(Reprinted from 33)**

Infrared microspectroscopy involves the optically interfaced microscope to a spectrometer in order to view a sample and analyze the exact same location. The infrared light travels along the same path as visible light in the microscope. When recording a spectrum, the visible light is simply shut off or covered so as to not interfere with the infrared beam. The applications range from the study of mis-folded protein diseases, such as Alzheimers, Huntingtons, Parkinsons, Mad Cow, Scrapie, and Creutzfedlt-Jakob disease **(34)**, to the *in situ* analysis of grains.

Infrared utilizers are always "fighting" to maintain the energy of the signal. The replacement of refractive objectives and condensers in a research grade microscope with cassegrainian mirror lenses (**Figure 1.7**), which have front surface optics that do not absorb infrared, was an important advancement along with avoiding slits in the spectrometer. Redundant Aperturing®, a confocal operation with an aperture before light goes through the lens and after it has gone through the sample and out the other lens, was necessary to produce spatial purity. With just one remote projected aperture, the light "crawls" around the target area and accidentally samples unwanted area outside the target. Because there is not spatial purity, the spectra of both the neighboring material as well as the target are collected. Spatial resolution is the name of the game, and the challenge is to sample the "sea of protein" with a bunch of boats, starch granules, floating in the sea. A more detailed description of infrared advancements can be found in the 1995 book chapter by Wetzel **(33)**.

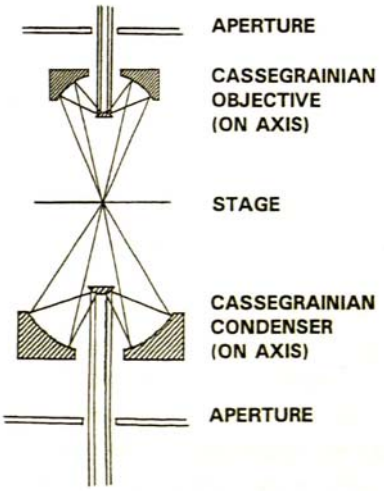

Figure 1.7: Diagram of a cassegrainian objective and condenser with apertures placed before the objective and after the condenser to achieve confocal operation. **(Reprinted from 33)**

The fundamental frequency of interest, in terms of endosperm hardness, is found in the amide I region. This region, centering around 1650 cm^{-1}, is characteristic of the C=O stretching vibrations in a protein molecule. Further down on the infrared spectrum lies the amide II and amide III bands. The amide II band is not as sensitive to structural changes. The amide III is sensitive, but, in terms of this study, is typically covered by vibrations from starch and hemicellulose **(35)**. When resolved using deconvolution, curve fitting, or a multivariate analysis, this peak reveals protein secondary structure. A peak for α-helix typically appears at 1650 cm^{-1}, while β-sheet appears around 1636 cm^{-1} (**Figure 1.8**). Another peak around 1670-1695 cm^{-1} has

also been attributed to the antiparallel β-sheet structure **(Figure 1.5a)**. However, in this region the β-turn structure and peaks characteristic of aggregation appear, and oftentimes overlap or combine with the non-prominent β-sheet structure **(37)**. While many proteins, such as bacterial membrane proteins shown in **Figure 1.8**, exist as primarily α- or β-, plant proteins are heterogeneous.

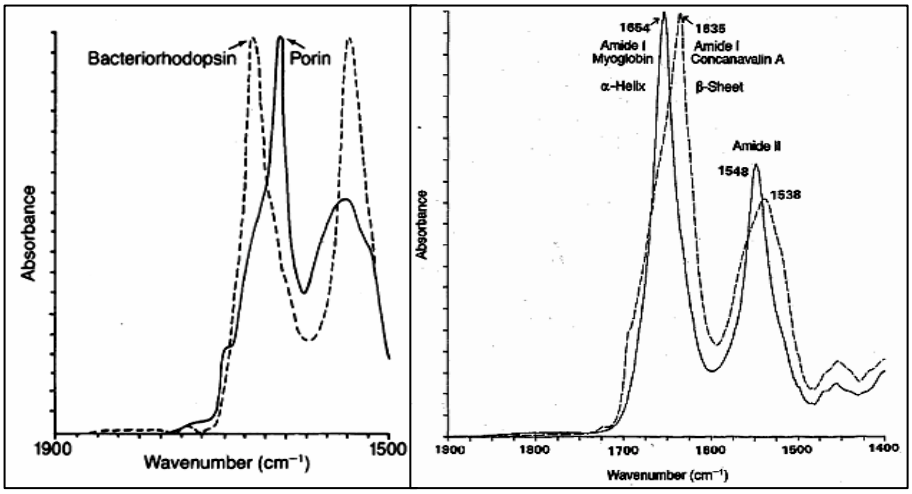

Figure 1.8: Model proteins consisting of mostly α-helix secondary structure (Bacteriorhodopsin and Myoglobin) or β-sheet secondary structure (Porin and Concanavalin A). **(Reprinted from 36)**

Raman spectroscopy is another vibrational spectroscopic method used to compliment infrared spectroscopy. Raman, as with infrared, has overcome some of the same issues with noise and high interference spectra through development of Fourier transform-Raman instruments and the use of near-IR lasers. Raman is advantageous due to the ability to use thicker specimens. As mentioned above, the use of confocal Raman microspectroscopy permits high spatial resolution **(11, 12, 13, 14, 15)**.

Recent applications have involved the determination of protein structure using the near infrared (NIR) spectrum **(38, 39, 40)**. These studies have looked at silk protein **(40)** and wheat gluten **(38, 39)**. Overall, NIR has an experimental advantage due to thick sample size, less interaction with water, and fast recording time, but, without use of fundamental vibrational bands, protein secondary structure study is completely dependent on chemometric statistical application. Therefore, future work is needed to enhance the application of this method.

Other Protein Structure Determination Methods: In nuclear magnetic resonance spectroscopy (NMR), the response of each proton nucleus to its environment in the molecule and proximity to other protons enables construction of models with configurations consistent with the

resulting NMR spectra. NMR allows interpretation of three-dimensional protein structure in solution and in solid state. It wasn't until the 1980s when the first three-dimensional protein structures were predicted **(41, 42)**. An extensive review **(43)** and literature **(44)** can be found regarding advancements in protein NMR spectroscopy.

In the early 1970s the analysis of amino acid side chain frequency of occurrence and location within known proteins' secondary structure, based on X-ray diffraction data, has been used to provide a means of predicting protein secondary structure for unknown proteins **(45)**. After development of a model, it was then used to predict the secondary structure of unknown protein structures with 80% accuracy **(46)**. This method was advantageous at the time due to its ability to side step computer generated algorithms. Although other attempts have been made to predict structure based on amino acid sequence, this has yet to be accepted as the primary method of analysis.

Physical Kernel Hardness Measurements

Physical tests based on particle size resulting from a standard grinding operation are commonly used in commerce for the determination of kernel hardness of bulk specimens: pearling index determined by the weight of abraded material from kernel surface produced after a specific amount of time at a specific speed **(47)**, particle size index measured by the amount of throughs collected from a set of sieves **(48, 49, 50)**, and the optical response diffusely reflected at select near IR wavelengths related to light scattering and penetration depth **(48, 51)**.

Miscellaneous tests were also employed. Wheat breeder, Mattern **(52)**, visual inspected crushed kernels under a microscope to assess hardness. Agricultural engineer, Massie **(53)**, uses a microphone to measure the acoustics during crushing of hard and soft wheat. Eilert **(54)** used photo acoustics to measure the sound output from pulsed light bombardment of hard and soft wheat kernels.

In commerce, careless mixing in grain handling or adulteration of hard wheat lots with lower cost soft wheat resulted in single kernel testing method development. The use of a force transducer to mechanically determine the resistance to crushing a kernel is known as the single kernel characterization system (SKCS) **(55, 56, 57)**. The commercial automated version licensed by the USDA and manufactured by Pertin Instruments is described under AACC Approved method 55-31 **(48)**.

Complete destruction of the wheat kernel remains the underlying disadvantage of all previously described methods. For this reason, *in situ* analysis of the wheat kernel offers advantages such as probing specific areas between the bran and central endosperm without the need for time-consuming fractionation. Mills et al. provided a complete review of *in situ* analysis of wheat kernels **(58)**.

Although physical methods have been used extensively, it is well known that physical resistance is not the determining factor in endosperm hardness. The chemical/molecular differences found in the endosperm of soft and hard wheat determines their end-use characteristics. Raman and mid-infrared studies previously discussed **(13, 14, 15, 16)** form the basis of the present study. It should be noted that most protein analysis has been done using protein in solution. *In situ* analysis offers the ability to study molecular differences of protein in its natural environment. Outside contamination and effects of heat, light and chemicals is reduced. With regard to endosperm hardness, the application of *in situ* analysis of wheat applies a molecular understanding to what was once thought of as a purely physical characteristic.

Experimental

Instrumentation

Fourier transform infrared (FT-IR) microspectroscopic data from the 2002 through 2005 crop year was obtained from beamlines U10B and U2B at the National Synchrotron Light Source (NSLS) at Brookhaven National Laboratory (BNL), Upton, NY. **Figure 1.9** is a diagram of the NSLS synchrotron with its two storage rings and beamlines. Electrons, **A,** in the synchrotron are accelerated to approximately 75 meV under high vacuum via a linear accelerator (LINAC), **B**. The accelerated electrons are then further accelerated in a booster ring, **C**, from which they can enter the X-ray storage ring or the vacuum ultraviolet (VUV) storage ring. After entering the VUV ring at approximately 750 meV, eight bending magnets send the electrons around the ring to one of 17 possible radiation extraction outlets. Radiation ranges from soft X-rays through the far infrared region. **Figure 1.10** shows the setup for the extraction of infrared light off of the VUV storage ring. M1 is a water cooled copper, laser mirror that provides Bremsstrahlung shielding as it absorbs soft X-ray and VUV radiation and reflects it at right angles from the incident beam. Mirrors 2-5 in **Figure 1.10** are used to direct radiation to the microspectrometer. Vacuum is maintained up to the KBr window. The compartment containing M4 and M5 are

purged with nitrogen. An evacuated pipe, 10 m in length containing KBr windows at each end, extends from the extraction area to another set of steering mirrors that direct the synchrotron beam through a KBr window into the FT-IR spectrometer and infrared microscope. The microscope and spectrometer are continuously purged with boil-off nitrogen **(33)**. The infrared beam follows the same path in the microscope as visible light that illuminates the specimen. This allows one to visually select the area to be mapped and collect spectra of the exact same area **(60)**.

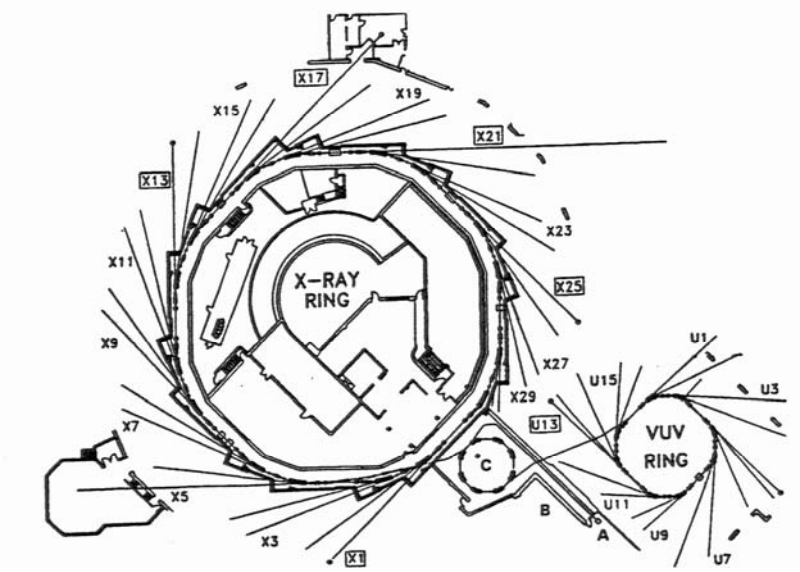

Figure 1.9: Diagram of the National Synchrotron Light Source storage rings and beamlines. A) electron source, B) linear accelerator, C) booster ring. **(Reprinted from 33)**

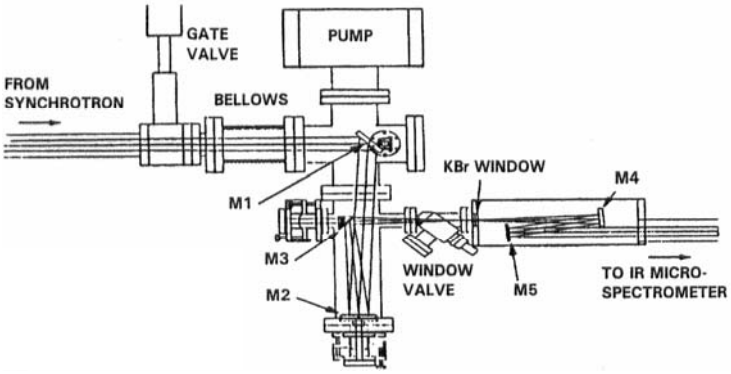

Figure 1.10: Mirror system between the synchrotron VUV storage ring and the IR microspectrometer. **(Reprinted from 59)**

Synchrotron light has three advantages over thermal sources. The light is approximately 100-1000 times brighter than a globar source, and because thermal noise is absent, a much higher

signal to noise ratio results. Unlike light from a filament that spreads in all directions, the synchrotron beam is highly directional which allows it to pass through a small projected image plane mask without seriously restricting the amount of light used for microspectroscopy.

Beamline U10B, **Figure 1.11**, is equipped with a Spectra Tech Continuμm® infrared microscope (Spectra Tech Instruments, Shelton, CT) having a matched pair of 32X, infinity corrected, Swartzchild objective and condenser, **Figure 1.12**. A 50 μm diameter MCT detector and an adjustable single mask with a double pass optical path provides confocal operation. Although the confocal feature restricts some of the light, it leads to improved spatial resolution. The Continuμm™ microscope is optically interfaced to a Nicolet Magnum 860 Step-Scan interferometer (Thermo-Nicolet, Madison, WI) equipped with a KBr beamsplitter.

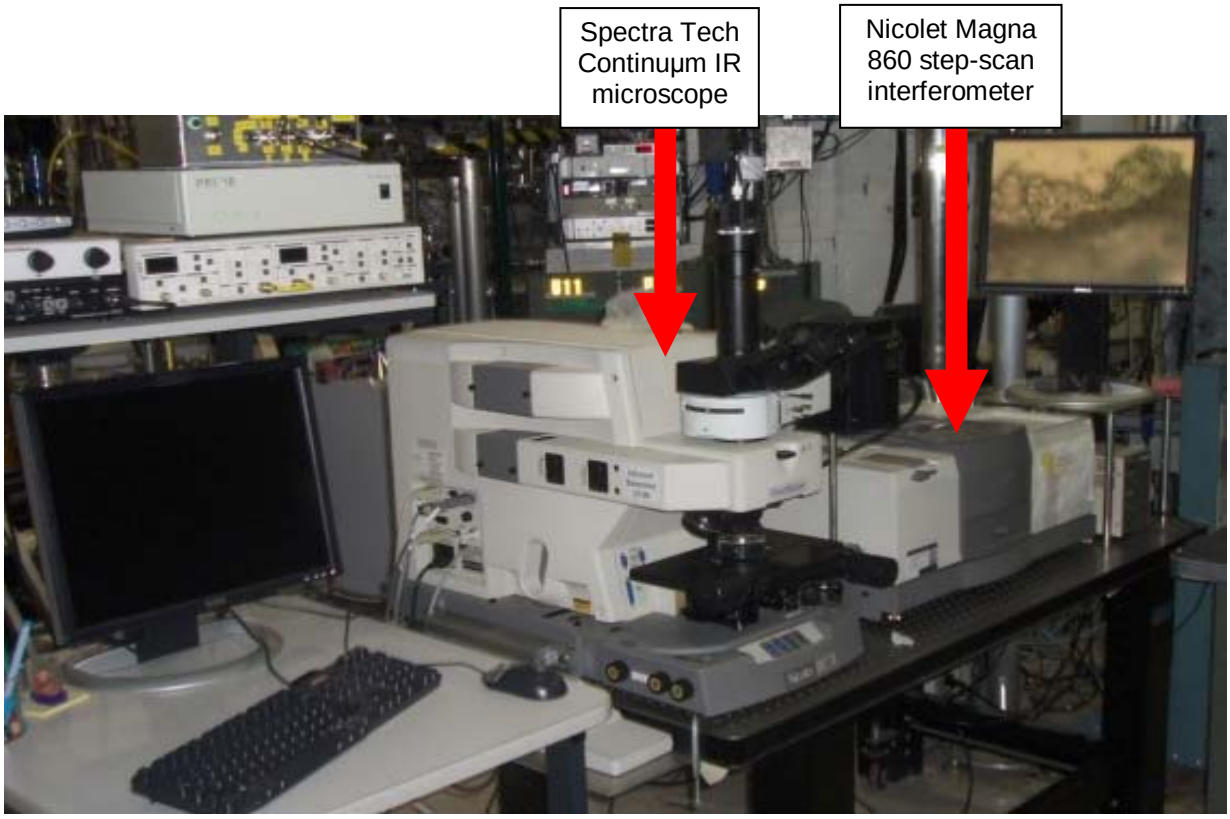

Figure 1.11: Spectrometer and microscope set up at beamline U10B at NSLS.

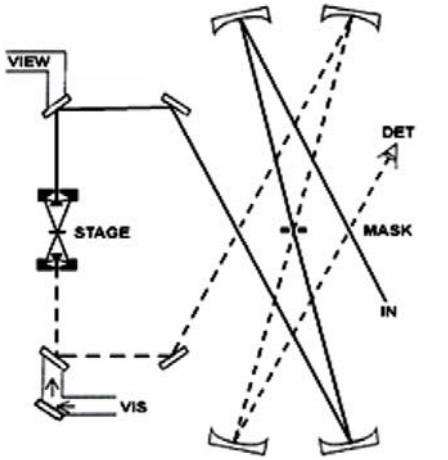

Figure 1.12: Diagram of matched 32X Swartzchild condenser and objective in the U10B instrument at NSLS with path of rays masked before and after microscope optics to operate confocally. **(Reprinted from 61)**

Beamline U2B, **Figure 1.13**, differs from U10B in that it contains a Nicolet NicPlan™ infrared microscope with 32X Swartzchild objective and 10X condenser. The NicPlan™ optical configuration differs from the Continuμm™ in that it has separate image plane masks before the objective and after the condenser, **Figure 1.7**. Before the objective, a pinhole mask was used that projected a 5 μm spot onto the sample. Below the stage, for these experiments, a larger circular mask was used that maintained the purge but did not restrict light directed to the detector. Both instruments were equipped with a programmable motorized stage.

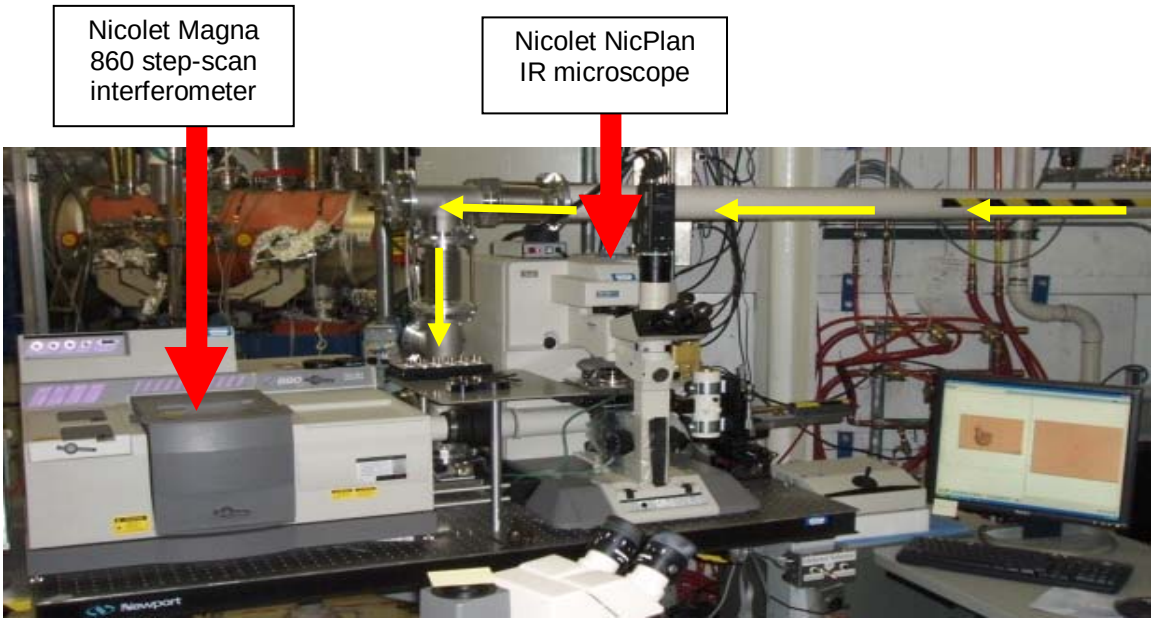

Figure 1.13: Diagram of the spectrometer/microscope set up at beamline U2B at the NSLS. Yellow arrows indicate the path of incoming synchrotron radiation from the VUV ring, through the beamline, and into the spectrometer.

During a time when it was not possible to schedule synchrotron beamtime, and to make it practical to develop local capability, an alternate FT-IR microspectrometer was employed for samples from the crop year 2006 at the Kansas State University Microbeam Molecular Spectroscopy Laboratory, Manhattan, KS. This same instrument was used for all protein film studies discussed later and for all endosperm microspectroscopy in 2007. Perkin-Elmer® (Shelton, CT) Spectrum™ Spotlight™ IR microscope optically interfaced to a SpectrumOne™ spectrometer, **Figure 1.14**, constituted the imaging system. The Spotlight™ infrared microscope was equipped with a liquid nitrogen cooled 16 element MCT array, a programmable motorized stage, and software to allow microprocessor controlled experimental setup and automated data acquisition. Unlike the Continuμm™ or NicPLAN™ microspectrometers, this imaging focal plane array (FPA) instrument does not employ image plane masks: see **Figure 1.15** showing the optical path. There is no image plane mask before the specimen, but the individual detector element projected onto the stage produces a nominal pixel size of 6.25 x 6.25 μm with the optics used for the endosperm experiments. For transmission experiments reported, 4000-800 cm^{-1} was used due to BaF_2 window limitations.

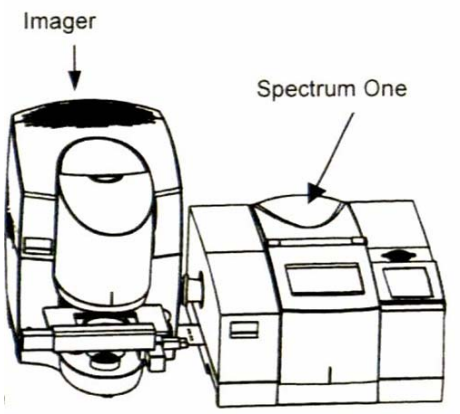

Figure 1.14: Diagram of the Spotlight and Spectrum One spectrometer and interferometer at the Kansas State University Microbeam Molecular Spectroscopy Laboratory. **(Adapted from 62)**

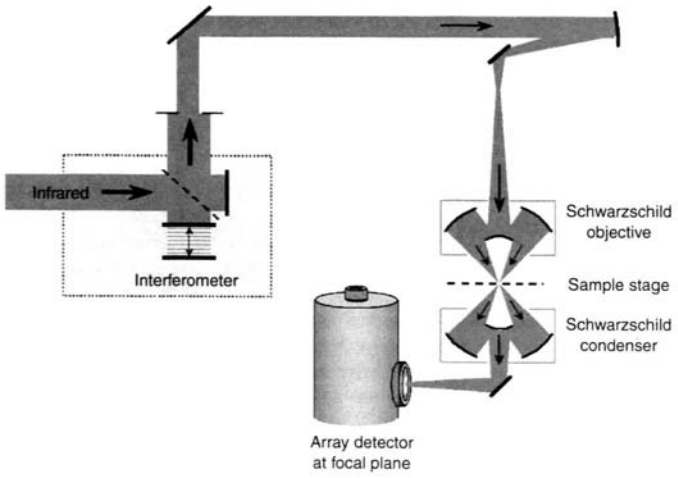

Figure 1.15: Diagram of the light path in a focal plane array instrument. The FPA instrument has no image plane mask in contrast to Figures 1.7 & 1.12. **(Reprinted from 63)**

Wheat Sample Preparation

Wheat samples consisting of both released varieties and experimental breeding lines were provided by Allan Fritz in the Agronomy Department at Kansas State University (Manhattan, KS). Experimental varieties were identified according to the nursery in which they were grown. Random numbering was assigned. Released varieties included Jagger, Jagalene, Overley and Santa Fe. These were controls for both the nursery and our experiment. Approximately 5-10 kernels were soaked in deionized water for a maximum time of 12 hours at refrigeration temperature. Individual kernels were frozen onto aluminum sample holders using OCT tissue freezing medium (Triangle Biomedical Sciences, Durham, NC), after which they were cryogenically sectioned into 4-6 μm thick slices. Slices were thaw mounted onto 1 mm thick, 13 mm diameter, BaF_2 windows for microspectroscopic analysis. Rectangular maps of wheat specimens typically 60-600 μm wide were mapped in transmission mode, resulting in 100-1000 pixels. Mapped areas were taken mostly from the subaleurone endosperm that is richer in protein and less crowded with light scattering starch granules, therefore resulting in a larger number of pixels from the interstitial region. Spectra from pixels high in protein relative to starch can be extracted for secondary structure determination. **Figure 1.16** shows a brightfield photomicrograph of wheat endosperm obtained from Dr. Yong Cheng Shi, Kansas State University, Manhattan, KS. This shows starch granules ranging from 5-30 μm. The interstitial protein areas between starch granules were preferentially selected for further analysis. Prior to

mapping a specimen, it was brought into focus on the infrared microscope stage to maximize the amount of light transmitted through the sample. Within a spectral range of 4000-800 cm^{-1}, a background, with coaddition of 256 using the synchrotron/Continuμm or 240 using the Spotlight, and a resolution of 8 cm^{-1}, in both cases, was used. Coaddition of 64 scans was used for the mapping procedure.

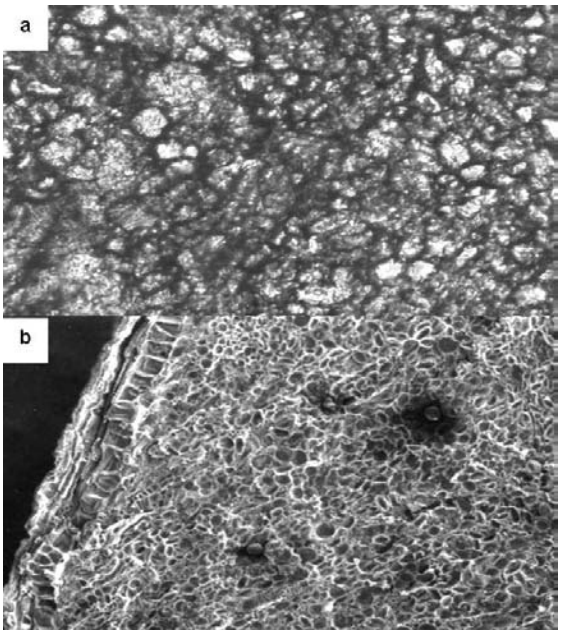

Figure 1.16: a) Brightfield photomicrograph of wheat endosperm section showing numerous starch granules from 30 μm to 5 μm in size. The scattering of light by the many starch granules attenuates the microbeam and reduces S/N of the spectrum that compromises interpretation of the data. Pixels from the interstitial protein were cherry picked for good baseline, low noise and a reasonable amide I band in comparison to the 1025 cm^{-1} starch band as described under experimental section. b) SEM photomicrograph of wheat slice showing starch granules closely packed together. (courtesy of Y.C. Shi)

Ten sections from ten individual kernels from two pairs of wheat samples, each pair consisting of one specimen from the 2005 crop year and one from the 2006 crop year, were mapped according to previously mentioned procedure to evaluate repeatability and kernel to kernel variance.

Pixel Selection

After mapping was complete, a false color image of the baseline corrected peak area ratio of protein, 1650 cm^{-1}, to carbohydrate, 1025 cm^{-1}, was produced using Omnic or Spotlight software. The resulting image enabled identification of protein rich pixels. A process referred to as "cherry picking"**(16)**, consisted of examining the spectrum each individual pixel to select

those for secondary structure analysis (See **Figures 1.17 & 1.18** showing photomicrograph data adopted from Mills et al. **(58)** to illustrate the difference in interstitial protein within the subaleurone and central endosperm, paired with spectra taken of the 2007 crop year wheat samples from the present study.). Distorted or off scale bands, drastically sloping baseline or high amounts of noise resulting from light scattering were all causes for spectral rejection. Spectra with a high amide I band at 1650 cm^{-1} compared to starch at 1025 cm^{-1} were selected for further analysis. To obtain quantitative information regarding the α-helix to β-sheet protein secondary structure, the spectra from 20-25 pixels of each mapping experiment were treated using a 3 step process consisting of definition, deconvolution, and peak fitting.

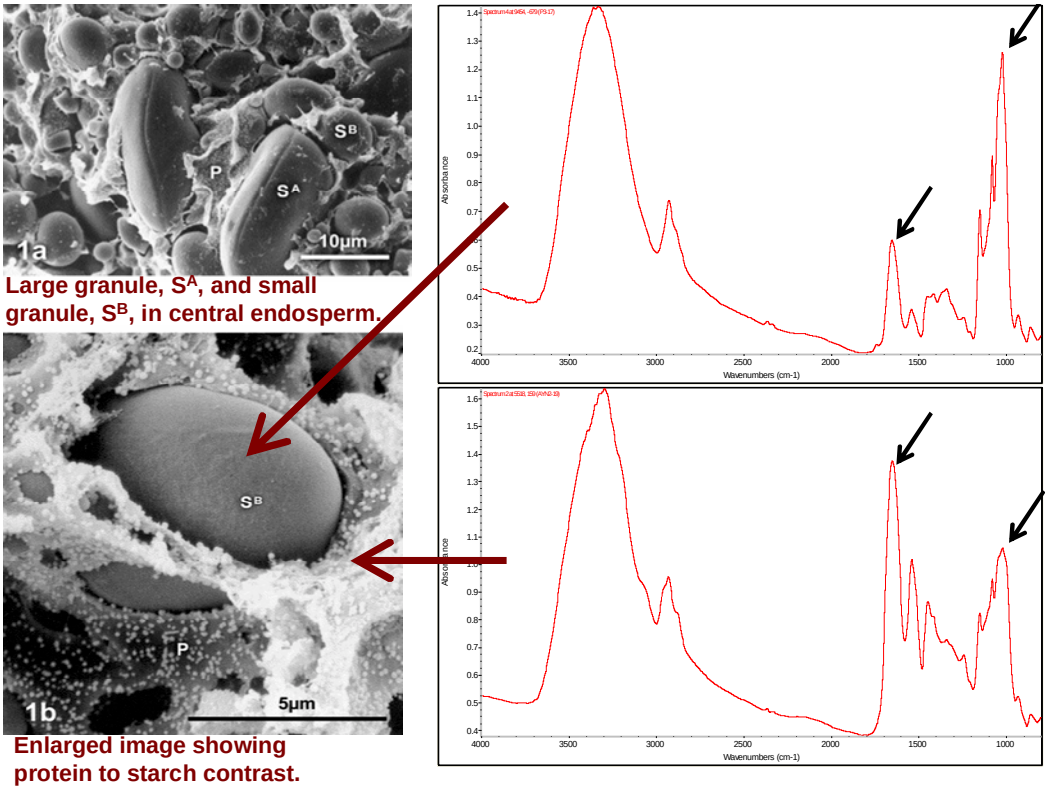

Figure 1.17: (Left) SEM photomicrographs reprinted from Mills et al **(58)** showing the central endosperm (Left, top) and the sub-aleurone endosperm (Left, bottom). Notice that there is significantly more interstitial protein in the sub-aleurone endosperm region. Specta (right) taken at the Kansas State University Microbeam Molecular Spectroscopy Laboratory showing pixels taken that are high in starch (Right, top) and high in protein (Right, bottom).

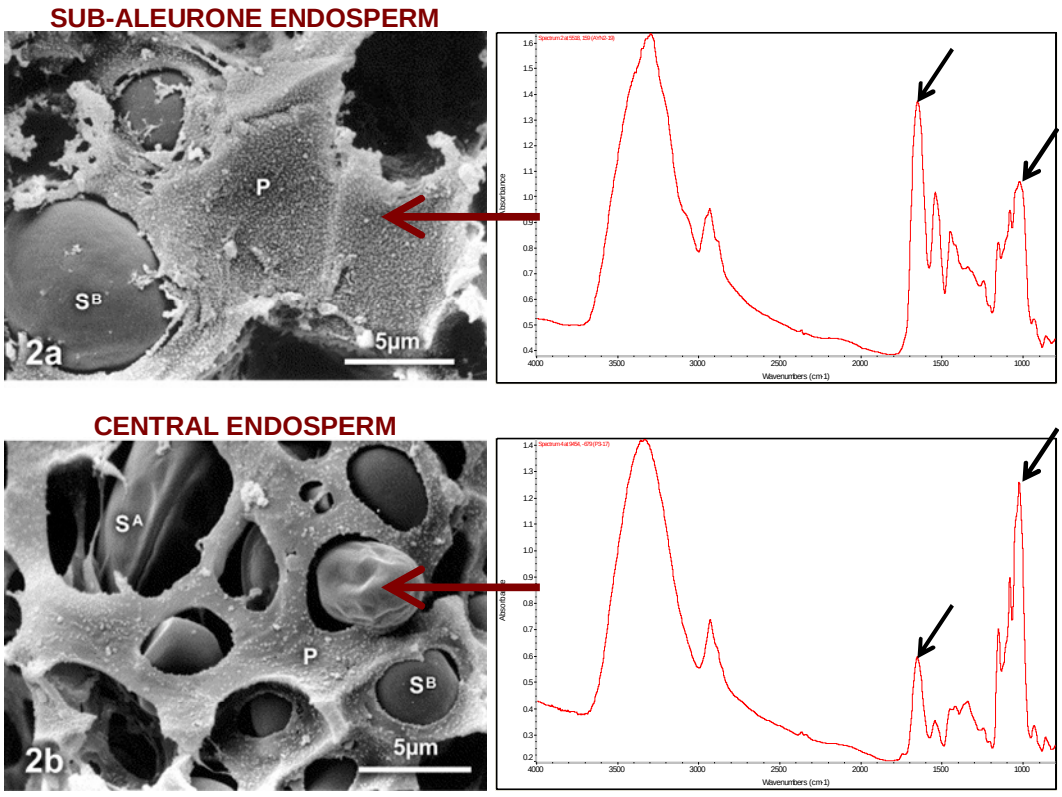

Figure 1.18: Photomicrographs of the sub-aleurone and central endosperm (left) **(Reprinted from 58)**, paired with spectra showing high starch (right, bottom) and high protein (right, top).

The use of an FPA instrument that is incapable of confocal operation sacrifices some spatial resolution achieved by the synchrotron, therefore, it was uncertain whether it was feasible to study interstitial protein. Synchrotron maps provided an abundance of pixels high in protein, so smaller maps could be taken, but pixel selection of a small map using the FPA instrument was less fruitful. The use of the Spotlight microspectrometer permitted the imaging of larger areas in the subaleurone region so more pixels were available for which to select spectra suitable for protein secondary structure determination.

Data Treatment

GRAMS "RAZOR" (ThermoGalactic, Salem NH) was used to achieve these three steps. First, the spectral range was reduced to 1570-1782 cm^{-1}. The peaks within the amide I were defined as having a Lorentzian shaped curve with a full width at half height of 20 and smoothed with 15 iterations. Deconvolution was performed using 60 iterations, followed by an automatic baseline correction. The Bayesian/maximum likelihood peak picker was used to identify individual peaks before a final peak fitting, which also used 60 iterations. Typically, three peaks

consistently fit within the spectra range at approximately 1680, 1650, and 1635 cm^{-1}. Various studies have reported the identification of these peaks as β-turn/antiparallel β-sheet, α-helix, and β-sheet protein secondary structure, respectively **(16, 24, 27, 37, 64, 65, 66)**. A peak around 1670-1695 cm^{-1} has also been attributed to the antiparallel β-sheet structure. However, in this region, the β-turn and other unordered structures appear and oftentimes overlap or combine with the non-prominent β-sheet structure **(37)**. For this reason, the β-sheet peak at 1635 cm^{-1} was used for comparison of secondary structure.

The area under the model of individual peaks generated at approximately 1650 and 1635 cm^{-1} was calculated and ratioed from the GRAMS "RAZOR" software. This generated a report that provided the approximate ratio of α-helix to β-sheet in a particular spectrum. Each individual spectrum selected from each specimen section was treated identically.

Results and Discussion

Heterogeneity of protein secondary structure exists within each map of wheat endosperm. The purpose of this experiment was not to determine exact values of endosperm hardness, but rather to rank wheat in terms of approximate endosperm hardness values. This is similar to an octane scale in that, when developed, the best fuel for an automotive engine was arbitrarily given a high value, and those that were less effective were given a lower value. In the same respect, this has been shown through analysis of a single kernel. The wheat showing the highest ratios are intended for use within frozen dough applications where the flour needs to be from hard endosperm, while those of middle or lower hardness rankings could be used in commercial bread products.

Preliminary work performed using synchrotron infrared microspectroscopy to analyze protein secondary structure in released varieties of hard and soft wheats has been reported by Wetzel et al. **(16)**. Results showed that the ratios of α-helix to β-sheet within soft wheat varieties ranged from 0.96 to 1.07, confirmed by others through secondary structure analysis of puroindolines-a and –b found in the protein matrix of soft wheat endosperm **(67)**. Analysis of hard wheat samples of released varieties grown side by side at the same test plot **(16)** produced values of a higher range: 1.57 to 2.10. This was in agreement with the results reported by Piot et al **(13)**. The present study applied the same testing with elimination of environmental factors within a given year.

Cultivars surveyed included current breeding lines in addition to released varieties used as a control. Samples within this study are from hard winter wheat class breeding lines coming from different nurseries operated by the Kansas Agriculture Experiment Station from six successive crop years. Released varieties, Jagger, Jagalene and Overley, were measured over four successive years, while Santa Fe for only three. **Figure 1.19** shows the two typical spectrums of hard and soft wheat. The top **(1.19a)** shows an α-helix to β-sheet ratio, close to 1, characteristic of soft wheat, while the bottom **(1.19b)** shows a higher ratio, characteristic of hard wheat varieties. On the other hand, **Figure 1.20** shows a comparison of modeled spectra taken from a very high ranked, hard wheat cultivar **(1.20a)** and a low ranked, semi hard wheat cultivar **(1.20b)**. The absorption spectrum in **Figure 1.20a** was taken from a wheat cultivar that resulted in an α:β ratio of 1.86, while the ratio from the wheat cultivar spectrum in **Figure 1.20b** was 1.36. The second derivative, although not the ultimate determinate of protein secondary structure identification, can be overlaid upon spectra to locate the peak positions at approximately 1656 cm^{-1} for α-helix and 1636 cm^{-1} for β-sheet.

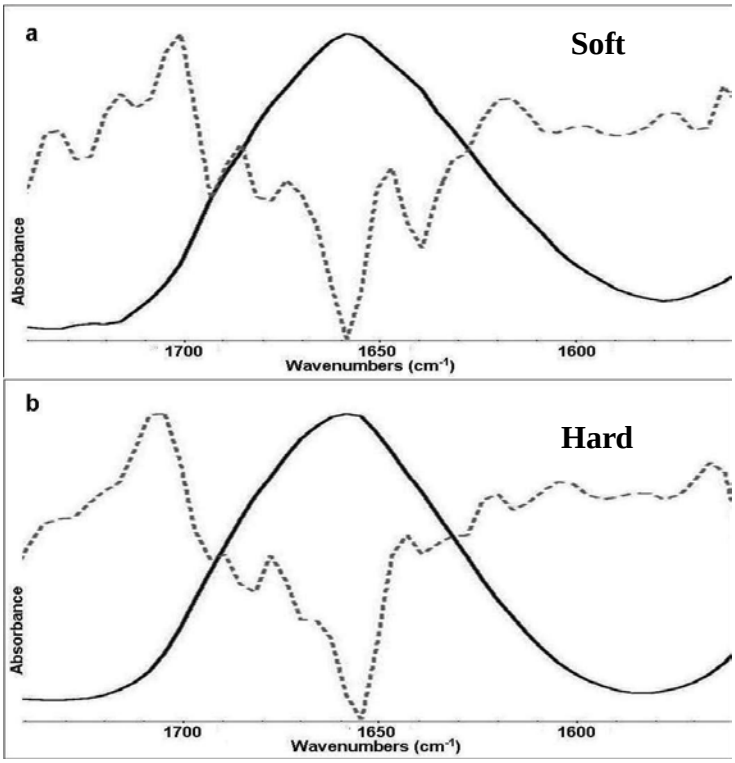

Figure 1.19: Figures a and b show differences in absorption spectra (solid line) second derivatives (dotted line) of the 1750-1550 cm^{-1} amide I region that result from the presence of different amounts of α-helix and other folded protein secondary structures, including β-sheet. Note the relative intensity of second derivative peaks at 1658 and 1630 cm^{-1}.

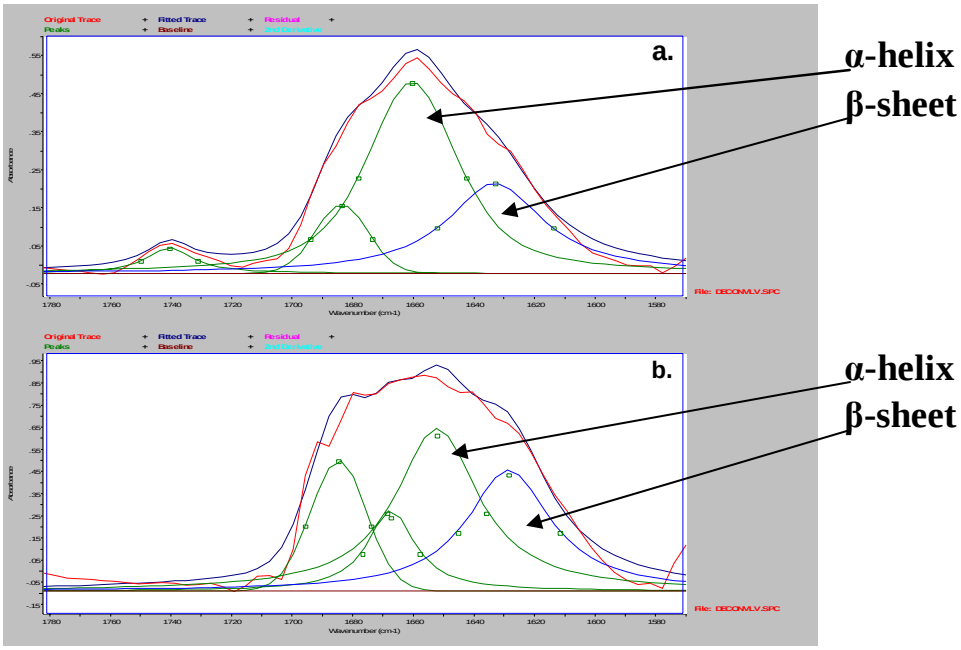

Figure 1.20: Figures a and b show differences in modeled spectra of the amide I region resulting from a wheat cultivar with an α:β ratio of 1.86 and 1.36 characteristic of a very hard cultivar and a semi hard cultivar, respectively.

In this study, the results are reported on 143 different experimental wheat varieties involving thousands of spectra. In each case, spectra from 20-25 pixels were selected from a 100-1000 pixel mapping procedure. For a given year close to 625 spectra were extracted and modeled individually to obtain α-helix to β-sheet ratios. Selection of spatially resolved pixels dominated by protein provided a basis for resolution enhancement. Modeling of α-helix and β-sheet absorption bands that contribute to the amide I band at approximately 1650 cm^{-1} was done for at least 1,500 spectra.

Ratios of α-helix to β-sheet for the 2002 through 2007 crop year are presented in **Table 1.1**. (Note that synchrotron data was used exclusively for all spectra prior to the 2006 crop year for which globar FT-IR FPA spectra were recorded as described under experimental.) The ranges and median values for the ratios of experimental lines are summarized in **Table 1.2**. The low amount of experimental wheat analyzed in 2007 was a result of losses due to late spring freeze and heavy rain during harvest in Kansas for the 2007 crop year. Therefore, the conditions also made the results less reliable.

Table 1.1: Alpha:Beta Ratios of Experimental Lines Over Six Years

Crop Year					
2002	2003	2004	2005	2006	2007†
			2.5	1.81	
	1.92		1.93	1.77	
	1.89		1.89	1.76	
	1.75	1.8	1.87	1.75	
	1.66	1.78	1.61	1.72	
1.72	1.6	1.77	1.59	1.67	
1.62	1.53	1.76	1.55	1.67	1.65
1.6	1.51	1.7	1.54	1.67	1.62
1.6	1.5	1.7	1.54	1.66	1.62
1.53	1.5	1.66	1.51	1.66	1.6
1.48	1.48	1.65	1.49	1.62	(1.54)*
1.47	1.47	1.65	1.48	1.62	1.38
1.46	(1.46)*	1.65	(1.47)*	1.59	1.36
1.45	1.45	1.62	1.46	1.55	1.34
1.45	1.45	1.61	1.43	(1.54)*	1.28
1.45	1.4	1.6	1.41	1.5	
1.45	1.4	(1.57)*	1.39	1.5	
1.41	1.36	1.57	1.38	1.48	
(1.39)*	1.32	1.54	1.37	1.48	
1.38	1.28	1.53	1.36	1.47	
1.37	1.27	1.53	1.33	1.46	
1.37	1.24	1.51	1.31	1.45	
1.35	1.24	1.5	1.31	1.39	
1.32	1.2	1.47	1.31	1.39	
1.32		1.47	1.3	1.38	
1.3		1.44	1.2	1.38	
1.27		1.38		1.36	
1.27		1.37		1.31	
1.24		1.35		1.3	
1.23		1.32		1.26	
1.23		1.11			
1.15					

† indicates values are less reliable due to field problems.

Table 1.2: Ranges from Successive Crop Years

Crop Year	High	Low	Median	n
2002	1.72	1.15	1.39	27
2003	1.92	1.20	1.46	23
2004	1.80	1.11	1.57	28
2005	2.50	1.20	1.47	26
2006	1.81	1.26	1.52	30
2007†	1.65	1.28	1.54	9

† indicates values are less reliable due to field problems.

All hard winter wheat lines tested were grown in Kansas Agriculture Experimental Station breeding program nurseries. It is interesting to note that although within a given year there was significant variation within experimental breeding lines coming from the same location where environmental factors were constant within that location. The idea behind this molecular testing method is to provide within hard wheat experimental lines a ranking of relative endosperm hardness. From year to year, with variations in environmental factors, it would not be expected that a given wheat would result in the exact same numerical value. Environmental factors play an important role in hardness measurement results **(68, 69, 70)**. A similar ranking for wheat varieties from year to year would, however, suggest the effects of genetic influence on expressed hardness.

The variation of approximately 0.75 units between the approximate α-helix to β-sheet ratio of soft wheat (1.00) and the average ratio of hard wheat (1.75), based on the previously reported values of Wetzel et al. **(16)**, within a year could be the result of the presence of puroindoline within soft wheat. Although the presence of puroindoline proteins is characteristic of soft wheat, it has been shown that several genetic mutations result in the expression of endosperm hardness **(7, 8)**. If puro-a and –b are present, however, they are in much lower concentration than in soft wheat. A mixture of puroindolines, having a 1:1 α-helix to β-sheet ratio **(67),** with protein in hard wheat of higher ratios would result in an overall lower average. This could partially explain the range within a set of hard winter wheat within a given year of the present study. This is purely speculation by the author and further analysis would need to be done in order to test this hypothesis.

Figure 1.21 shows the results from the single 2002 crop year in bar graph form (solid α-helix, open β-sheet). Higher integrated areas of α-helix and β-sheet curves merely reflect the sample thickness, whereas the relative population reflects the molecular measurement of endosperm hardness **(13, 14, 15)**. The wide range of resultant hardness values allows the breeder to select experimental cultivars, compare the new lines to released varieties, and make judgments regarding the end use of a particular wheat cultivar. Six breeding lines were compared over two successive crop years, shown in **Table 1.3**. Well-known released hard wheat varieties tested over three to four successive years serving as controls for experimental lines are compared in **Table 1.4**.

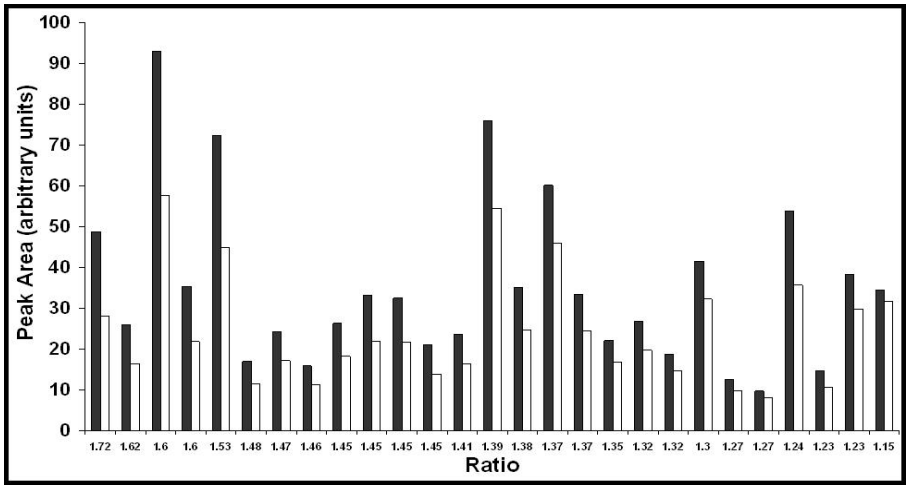

Figure 1.21: The bar graph is in descending order by α-helix to β-sheet ratio from left to right representing hard winter wheat specimens from the same nursery in a single crop year. Differences in peak area result in slight sample thickness variability.

Table 1.3: Ratios and Ranks for Two Successive Years

Wheat Cultivars	Relative α	Rank Agreement	Ratios ('05, '06)	Rank ('05, '06)
A	Highest	Different	2.50, 1.66	1,4
B	2nd highest	Close	1.69, 1.75	2,1
C	3rd highest	Close	1.55, 1.72	3,2
D	Mid	Similar	1.39, 1.67	4,3
E	Low	Similar	1.20, 1.62	6,5
F	Low	Similar	1.38, 1.30	5,6

Among the seven reported only A shows lack of consistency in reference to either rank or numerical value.

Table 1.4: Results for Known Wheat Cultivars Over Four Years

Cultivar	2004	2005	2006	2007†
Jagger	1.32	1.49	1.48	1.6
Jagalene	1.44	1.54	1.67	1.38
Overley	1.78	1.89	1.31	1.34
Santa Fe		1.48	1.45	1.62

† indicates values are less reliable due to field problems.

Note that good agreement was found in three successive years for Jagger and Jagalene. Santa Fe and Overley were in agreement for two successive years. Results for Overley differ in the third year. Controls **(Table 1.3)** grown provide a yearly basis of comparison for the

experimental lines reported in **Table 1.2**. Wheat variety A was higher or equal to control varieties Jagger, Jagalene, Overley and Santa Fe for two successive crop years, while variety F was consistently lower than all four. Wheat varieties B and C were consistently higher than control varieties Jagger, Jagalene and Santa Fe. For two successive crop years varieties D and E were both lower than or equal to Jagalene. (Data from the 2007 crop year, although listed, was not considered in this evaluation based on the unreliable results.)

From the experimental breeding lines that were repeated over two successive years, ten kernels were randomly selected from those considered to be high in α-helix, Variety A, and the low, Variety F, for further sectioning and data collection. The results from **Table 1.5** show that for both crop years Variety A is still, in fact, ranked higher than Variety F. There is a rather large standard deviation within the four varieties, the largest being that of the higher ranked wheat variety pair. Piot et al. **(14)** minimized this variation in his experiments by selecting kernels from the same location on the head of the wheat plant. He concluded that there was 5% variation in wheat kernels chosen from the same location on the head. Considering that 5% variation is the case, then even higher variation throughout the head should be expected. For future applications, careful selection of the wheat kernel location within the head is expected to reduce variability in the results.

Table 1.5: Kernel to Kernel Variation from Two Experimental Varieties over Two Successive Years

	Cultivar A		Cultivar B	
Kernel Number	2005 Crop Year	2006 Crop Year	2005 Crop Year	2006 Crop Year
1	2.50	1.66	1.38	1.30
2	1.37	1.79	1.39	1.68
3	1.42	1.67	1.70	1.61
4	1.34	1.44	1.40	1.52
5	1.42	1.11	1.40	1.18
6	1.66	1.28	1.26	1.47
7	1.54	1.78	1.34	1.32
8	1.34	1.49	1.53	1.55
9	1.58	1.50	1.41	1.46
10	1.48	1.44	1.46	1.27
Average	1.57	1.52	1.43	1.44
St. Dev	0.35	0.22	0.12	0.16

The molecular testing of known and experimental wheat breeding lines has been shown to rank samples in terms of endosperm hardness for both specific end use and as a basis for

breeding selection. Although, for decades, wheat kernel hardness was the only basis of testing in commerce. Kernel hardness, characterized by physical testing, is the manifestation of endosperm hardness that makes possible those somewhat rudimentary physical tests. By elimination of environmental differences through analysis of wheat cultivars from the same nursery within a given year, the genetic variation among varieties can be studied.

Chapter 2- Revelation of Secondary Structural Changes in Protein Films with Thermal Processing: Novel FT-IR imaging of protein film secondary structure by reflection absorption before and after heat treatment.

Literature Review

Thermal denaturation of proteins has been a subject of interest for decades. Thermal processing treatments such as extrusion, canning, pasteurization, and baking all benefit from analytical tools used to assess changes within the molecular composition of the product. Past studies have been limited to the heating and analysis of protein in solution, or through the analysis of films via attenuated total reflectance (ATR) infrared spectroscopy. This study aims to study the changes resulting from thermal denaturation of protein through FT-IR microspectroscopic imaging of the same films before and after treatment.

FT-IR Thermal Protein Denaturation Studies

Infrared spectroscopy of heat treated globular proteins dates back to the 1950's through the analysis insulin, chymotrysinogen, and glyoxalase **(71)**. Using FT-IR to study the changes upon thermal processing of globular proteins was first used by Clark et al. **(72)** to study the changes in bovine serum albumin, lysozyme, insulin, ribonuclease, and alphachymotrypsin in solution. Boye et al. **(73)** studied whey protein concentrate in solution. Payne and Veis **(74)** compared the location and width of the bands within deconvolved spectra of collagen and gelatin upon heating. Heating of pig citrate synthase **(37)** showed that the content of β-sheet increased upon heating while the amount of α-helix decreased. β-lactoglobulin, upon heating, aggregates and thus exhibits peaks within the amide I band near 1617 and 1682 cm^{-1} **(75, 76)**. This is common to all thermal studies **(37, 72, 74, 77)** with heating there is an increase of intermolecular antiparallel β-sheet that appears in the 1670-1680 cm^{-1} region and/or the 1620 cm^{-1} region. **Figure 2.1** shows the results of thermal denaturation of myoglobin **(77)**. One can clearly see that there is a peak that appears around 1620 cm^{-1} upon heating.

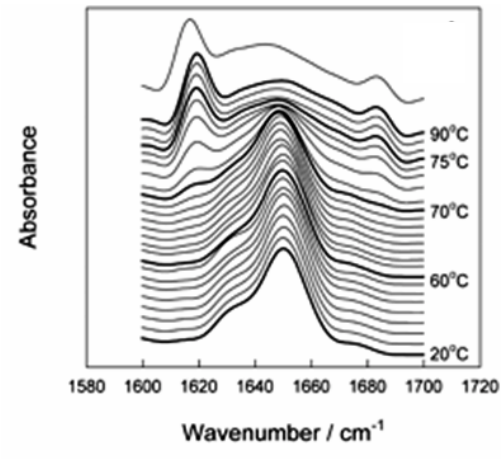

Figure 2.1: Spectra of the amide I region of myoglobin in solution heated to increasing temperatures **(Reprinted from 77)**. Notice the gradual appearance of a peak at approximately 1620 cm^{-1}.

Recent studies using ATR FT-IR examined the effects of hydration and temperature on wheat gluten. No changes in secondary structure were seen in the control, dry sample that was heated. It was interesting to note that no changes in secondary structure upon heating were seen below 45 ˚C. The glass transition temperature is approximately 45 ˚C. At medium hydration, 13% the change in secondary structure was reversible upon cooling, but not as much with 47% moisture content **(65)**. Recently reported near-infrared studies on gluten powder confirmed that upon denaturation the amount of α-helix decreased and was converted to β-sheet **(39)**. Spray-drying, pasteurization **(78)**, and extrusion **(79)** effects on soy protein showed that the amount of alpha-helix was depleted while that of β-sheet and random coil increased as a result of high temperature treatment.

Thermal Denaturation of Films

Changes in protein secondary structure during film formation have been recognized **(80)**, but the exact changes across the entire film have yet to be fully understood. ATR FT-IR spectroscopy is commonly used for the analysis of films **(24)**. ATR requires direct optical contact of the sample with an IR transparent crystal that has a high index of refraction, therefore sample thickness is not an issue. There is a critical angle beyond which all of the light is reflected which makes ATR analysis possible. ATR is disadvantageous due to its inability to image a sample and it is unclear whether there is interaction with the crystal **(24)**. The use of a diamond ATR crystal, however, removes the possibility of crystal-sample interaction. It was

confirmed in 1992 using ATR FT-IR that the spectra on thin films differed from those of protein in solution. Furthermore, hydrated films differed from completely dry films **(80)**.

Although it was not called "ATR" at the time, one of the first uses of ATR was the study of zein films **(81)**. Zein films were deposited on silver chloride plates and ATR analysis were performed with a sodium chloride prism. Goormaghtigh et al. **(82)** also studied films using ATR FT-IR. Various proteins were analyzed and secondary structure, computed by deconvolution and curve fitting, showed a mere 8% standard deviation from X-ray diffraction data results. The effects of film formation on glycinin revealed that during the film drying process, β-sheet aggregates form. The authors hypothesized that the beta-sheet aggregates act as nuclei, forming the base of the film **(83)**. Mangevel et al. **(66)** studied the structure changes of wheat gliadins upon film formation. It was shown that upon drying at low temperatures, β-sheet aggregates form, with the amount increasing (8- 25%) with increased drying temperature (25-90 ˚C).

Effects of Thermal Treatment on Protein Structure

Due to the flexibility of the polypeptide chain and due to amphipathic properties, proteins are able to change conformation and stabilize films through air-water and air-surface interactions **(19)**. Evaporation of water leads to breaking and reforming of hydrogen bonds causing a change in secondary structure. To use the least amount of energy, the hydrogen bonds quickly unite at the shortest distance possible. Therefore the appearance of a peak at a lower frequency (about 1620 cm^{-1}) and, in some cases a side lobe at higher frequencies (approximately 1685 cm^{-1}) is a common sign of aggregation **(24, 66, 72, 77)**. Jackson and Mantch **(24)** also state that a peak forming greater than 1670 cm^{-1} or greater is due to the case of electron density being weighted toward the carboxyl portion of the peptide bond thus preventing it from hydrogen bonding. This creates a peak shown at this higher frequency.

This study introduces a novel approach to microspectroscopically document protein structural changes induced by thermal treatment. Through the casting of films onto a highly polished stainless steel surface, reflection absorption microspectroscopy enables analysis of the exact same film location before and after heating. Myoglobin was chosen as a model for method development based on earlier work done in solution **(77)** due to its relative secondary structural homogeneity and natively high α-helix content. The molecular model was applied to gelatin,

another animal source, while wheat gluten was used to represent a plant source. This study has been restricted to the soluble portion of each sample to avoid dealing with more complex insoluble organic materials.

Experimental

Model Protein Selection

To follow the conversion of α-helix to other secondary structures a material high in α-helix secondary structure and relatively homogeneous was sought. Preliminary experiments were attempted with large 1-2 cm diameter protein films deposited from a glass dropper on infrared reflecting glass. Soy protein isolate, soy protein concentrate, whey protein isolate, edible gelatin, gelatin capsules, oat protein, wheat gluten, corn gluten, myoglobin, tofu and extracted soy and oat protein were some of the materials tested for feasibility. The inability to randomly select spectra with consistent results on the infrared reflecting glass led to speculation that the tin oxide layer of the glass caused a surface effect with the protein. To avoid surface attraction films were then cast on Teflon to be peeled off allowing spectra to be recorded in a transmission mode. Transmission was limited to the outside of most films. The ability to peel films off of the Teflon surface that were thin enough to let infrared light through was nearly impossible. Smaller protein films reduced solvent evaporation time and allowed mapping of the entire film. Polished stainless steel provided an uncharged infrared reflecting substrate for reflection absorption imaging.

After several preliminary investigations, myoglobin was chosen for method development as a model suitable for the study of protein secondary structure changes after thermal processing. Myoglobin had been identified in the past as existing a primarily an α-helical protein **(36, 37, 77, 84**).

Instrumentation

All films were imaged using the Perkin-Elmer® (Shelton, CT) Spectrum™ Spotlight™ IR microscope optically interfaced to a SpectrumOne™ spectrometer, **Figure 1.14**, at the Kansas State University Microbeam Molecular Spectroscopy Laboratory in Manhattan, KS. Refer to chapter 1 regarding detailed information on optical setup.

Protein Film Sample Preparation

Myoglobin was the raw material chosen to demonstrate protein secondary structure changes during thermal processing. Horse skeletal muscle myoglobin was obtained from Sigma Aldrich (St. Louis, MO) claiming 95-100% purity. As described previously **(85),** myoglobin was dissolved, 5% w/w, in 0.01M phosphate buffer. Phosphate buffer was prepared by mixing 0.01M K_2HPO_4 and 0.01M KH_2PO_4 in approximately a 0.99:1.00 ratio until the pH measured 6.8. Dissolved myoglobin was filtered with a Millipore® 0.5 μm filter fit into a Sweeney adaptor connected to a 2 mL ground glass syringe. Using a 3/10 mL syringe with a 31 gage syringe, two drops of myoglobin were deposited onto polished stainless steel plates and allowed to dry at room temperature. This procedure produced a 500 to 1500 μm diameter film with suitable thickness to allow reflection absorption. Samples were stored in a humidor from 30 min to overnight before infrared analysis.

Materials chosen for applying the technique developed to an animal and plant source were gelatin and wheat gluten (WG), respectively. Gelatin was produced in capsule form by Eli Lilly and Co. (Indianapolis, IN). The gelatin capsule, 0.07 g, was stirred continuously until complete dissolution in 10 mL deionized water at pH 7.0. Gelatin was filtered in the same way as myoglobin only with the use of Whatman #1 filter paper. Four drops of filtered gelatin were deposited onto the stainless steel plates for imaging.

WG, approximately 80% protein, was obtained from MGP Ingredients, Inc. (Atchison, KS). For three films, one gram of WG was mixed into 10 mL of deionized water, pH 7.0. The mixture was shaken for 2 min, centrifuged using an IEC CU-5000 centrifuge (Needham Hts, MA) at 2500 rpm for 10 min and the supernatant was recovered.

Alternate solute was utilized for additional WG films. For one pair of films, pretreatment involved grinding the WG with a mortar and pestle before adding deionized water and, alternatively, another pair of films was produced by shaking the non-ground WG for a total of 30 min before centrifugation to see if additional solubility resulted. Filtering was performed with the same apparatus used for myoglobin, and three drops were deposited onto the stainless steel plate.

Imaging

Films were imaged using the Spectrum Spotlight, described in chapter 1. After a background spectrum was collected from the polished plate, reflection absorption measurements of the entire film over 4000-800 cm^{-1} were imaged with 240 and 64 scans, respectively, with a 25 μm image plane mask. Film ranged from 500 to 1500 μm in diameter resulting in up to 4000 spectra. Twenty spectra near the center of each of seven films were evaluated before and after heating for each of three different protein sources for repeatability purposes and to produce a good data base.

Film Heating

Thermal processing was done in the presence of water vapor to maintain hydration to allow changes in protein secondary structure to proceed during heating. After completion of initial imaging, the films, mounted on their respective stainless steel plates, were placed in a glass Petri dish (9 cm diameter) containing a watch glass (6 cm diameter) to keep the plate above the water level. Approximately 10 mL of water was poured into the bottom of the dish. A large watch glass (15 cm diameter) was fit over the Petri dish containing the plate and the entire apparatus was heated for 30 min at 100 ˚C. **Figure 2.2** shows a diagram of the setup used for heating. After heating the plate was removed and allowed to cool and dry at room temperature for a minimum of 30 min before imaging of the same film using parameters previously described. **Figure 2.3** shows the visible image of a myoglobin, WG and gelatin films before and after heating. In all cases the entire film was imaged.

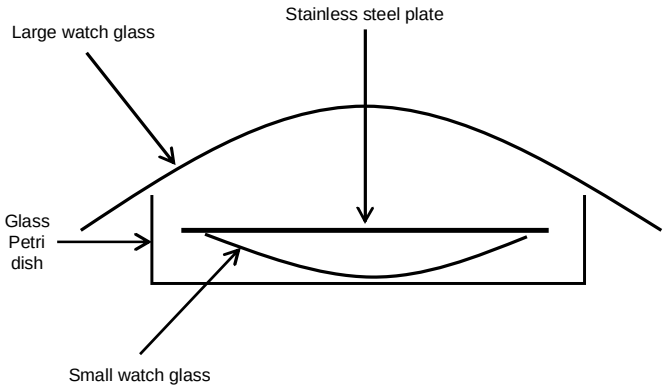

Figure 2.2: Diagram of the apparatus used for heating protein films on a stainless steel plate.

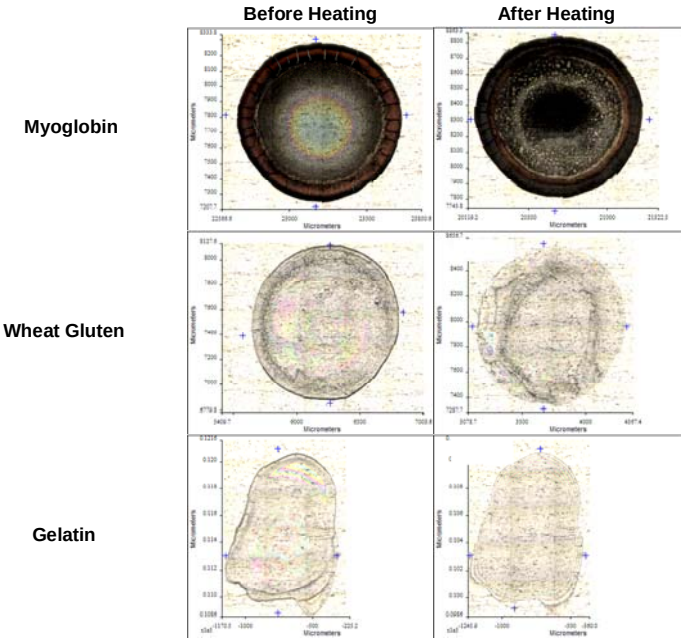

Figure 2.3: Microscopic images produced using the Spotlight microspectrometer. Films of the model, myoglobin, and applications, wheat gluten and gelatin, are shown before and after heating.

Pixel Selection

False color images of the baseline corrected peak area ratio of protein, from the 1736 to 1500 cm^{-1} region, were produced using Spotlight software to highlight the central area of relatively homogeneous spectra. Areas high in protein absorbance, typically along the outer ring of the films, were assigned a red color, indicative of aggregation. Twenty spectra from the center most area of each of seven films were selected for study. Pixels were rejected if their spectrum baseline was slanted or showed a high amount of interference due to a gap between the film and the stainless steel mirror surface. The center of a few of the films bubbled up after heating, which was apparent from their spectra and through visual inspection. When this was the case, spectra were extracted from the perimeter of the bubbled area, but within the center of the film. Using Omnic 7.3 software 20 spectra per film were averaged and the peak maxima location of all 20 spectra and averages were recorded.

Data Treatment

Second derivative, deconvolution and peak fitting were performed on each averaged spectrum using GRAMS AI, 7.02 (Thermo Galactic, Thermo Scientific, Waltham, MA). The spectral range was reduced to 1782-1570 cm^{-1}. The second derivative using the 2^{nd} order and

seven smoothing points identified the position of individual peaks. Each spectrum was deconvolved between 1782 and 1570 cm^{-1} using a gamma factor of 7.5, value based on experience from previous studies **(86)**. A mixed Gaussian and Lorentzian function was used to model peaks within the deconvolved spectra using low sensitivity, an offset baseline function, and a full width at half height (FWHH) of 13 **(64, 86)**. Peaks were fit using 50 iterations. Areas under the model corresponding to α-helix, 1650-1660 cm^{-1}, were ratioed to areas of the β-sheet model, 1630- 1640 cm^{-1}, β-turn/intermolecular antiparallel β-sheet, 1670-1685 cm^{-1}, and all peaks other than α-helix summed together.

Results and Discussion

Myoglobin

It is evident from the film image results that it is possible to study the effects of thermal processing on the exact same film deposited on an uncharged reflective substrate. It is widely know that myoglobin exists primarily in an α-helical secondary conformation **(36, 37, 77, 84)**. In fact, X-ray crystallographic data confirms that myoglobin consists of over 80% α-helix **(87)**. For this reason, the relatively homogenous myoglobin was chosen as a model system to study the effects of thermal processing on protein secondary structure. Twenty spectra from one myoglobin film, in common scale, are overlayed in **Figure 2.4** to show the homogeneity of myoglobin before heating. **Figure 2.5** shows false color images of the 4th myoglobin film before and after heating. Notice that there is a red ring around the outside perimeter of the film. This area is characterized by thicker film deposition where a shift of the amide I band is observed. The spectra within the center of the film, the dark blue region, have approximately at same amide I peak location. A typical spectrum from the outer red ring is overlaid upon a typical spectrum from the inner blue region in **Figure 2.6**. As the film dries there is a constant breaking and reforming of hydrogen bonds between neighboring protein molecules, air, and surrounding water. Since the outside ring is the first to dry, the protein apparently accumulates and self assembles, possibly as intermolecular antiparallel β-sheet or β-turn consistent with the higher frequency band. To simplify the study, the spectra from the homogenous center of the film without regard to the apparent build up at the edge of the film during solvent evaporation.

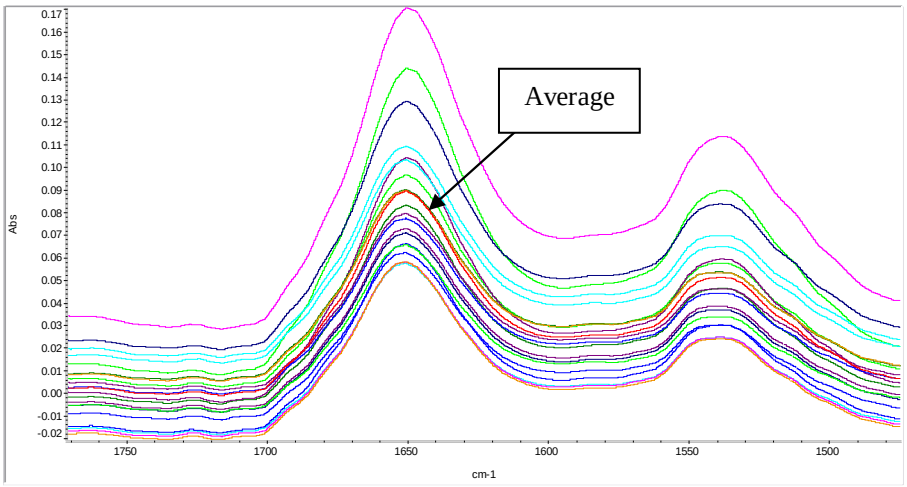

Figure 2.4: The amide I, II region of twenty spectra and the average (red) of a single myoglobin film, before heating, in common view. The spectra in the amide I region appear and the exact same peak maxima, indicating high homogeneity of myoglobin before heating.

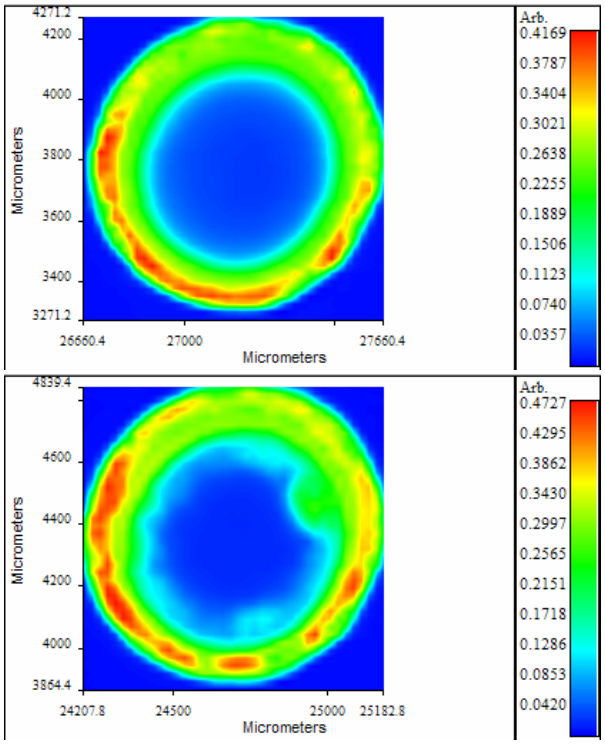

Figure 2.5: False color images of a single myoglobin film before heating (top) and after heating (bottom). Colors depict high protein absorption. (amide I and II region)

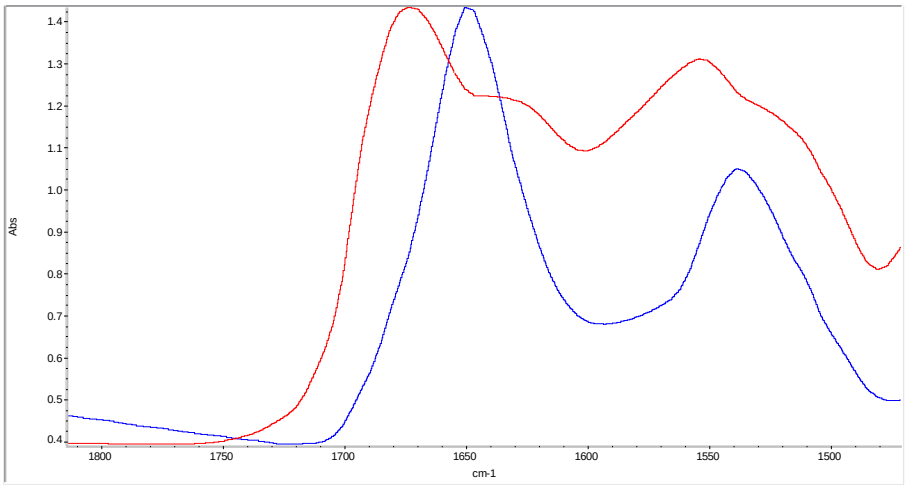

Figure 2.6: A typical spectrum of the amide I, II region representing the center of an unheated myoglobin film (blue). A typical spectrum resulting from self assembly at the outer edge of the film (red). Spectra from the outer edge were not included in the scope of this study.

Twenty spectra from each of seven different films of myoglobin before heating were compiled into the histogram shown in **Figure 2.7**. It is easy to recognize that the distribution is very tight, most of the spectra showing peak maxima at 1652 and 1648 cm^{-1}. The peak height location does correlate well with previous studies **(36, 37, 77, 84)**. Upon heating the amide I band reveals a peak maxima shifted to either a higher or lower wavenumber with a distinct visible shoulder. **Figure 2.8** shows the averages from 20-21 spectra of seven unheated films and seven heated films. Histograms of the amide I locations of main peaks, **Figure 2.9**, and shoulder peaks, **Figure 2.10**, after heating show a wide distribution compared to that of the unheated spectra. Notice in **Figure 2.10** that the majority of the spectra have shifted to lower wavenumbers, approximately 1625-1630 cm^{-1}, while a substantial portion has also shifted to wavenumbers above 1655 cm^{-1}. During the heating process, proteins unfold. Upon cooling the hydrogen bonds quickly reunite to maintain the most stable conformation in the shortest amount of time. In order for this to occur, β-sheet aggregates are favored over alpha-helical secondary structures. Previous studies of myoglobin in solution **(77, 84)** have shown that upon heating, the peak location shifts to approximately 1620 cm^{-1} with additional side lobes at 1685 cm^{-1}. This implies the formation of intermolecular β-sheet aggregates. The present study is in agreement with these findings. In addition, the formation of intermolecular antiparallel β-sheet at around 1670-1680 cm^{-1} **(37, 72, 74)** have been reported in other proteins.

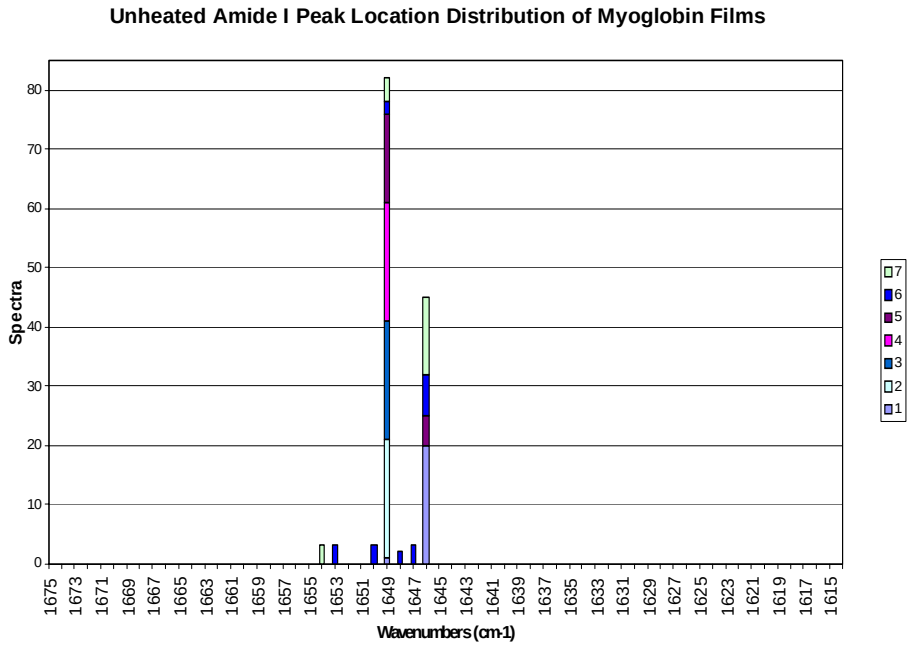

Figure 2.7: Accumulation of the amide I peak maxima values for all 140 spectra from seven, unheated myoglobin films such as those in **Figure 24**.

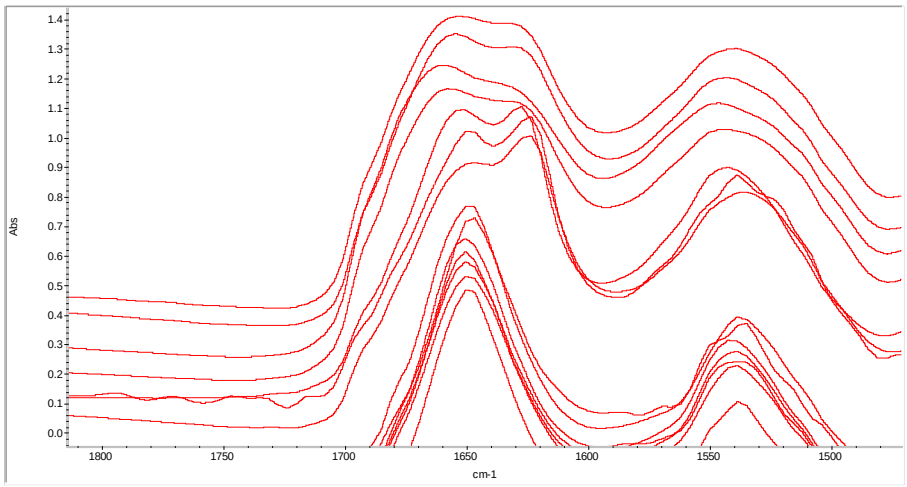

Figure 2.8: Amide region from 14 average spectra each from 20-21 individual spectra selected from seven different myoglobin films: seven unheated (bottom spectra) and seven heated (top spectra).

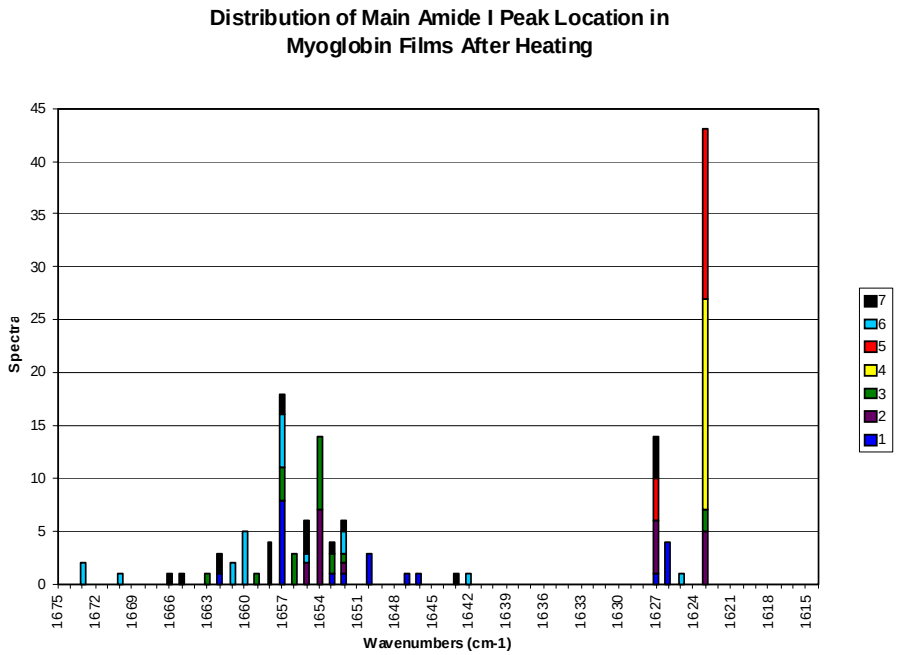

Figure 2.9: Accumulation of the amide I peak maxima of 140 spectra taken from seven myoglobin films heated to 100 ˚C for 30 min.

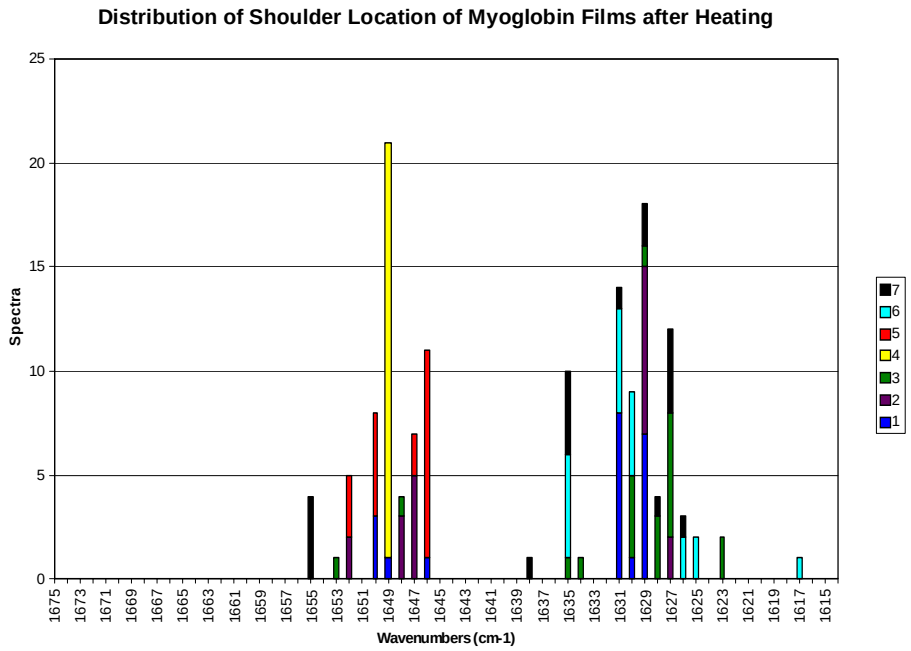

Figure 2.10: Amide I peak location of the shoulder found on spectra from heated myoglobin films, taken from 140 spectra in seven films.

It is interesting to see that the shoulder location distribution has shifted almost completely to lower wavenumbers, while approximately 12% of the shoulders stayed at the same location as

the original, unheated protein (**Figure 2.10)**. This indicates that there is not a uniform conversion from one secondary form to another, and when the main peak was shifted to a higher wavenumber, a slight amount either stayed in the same spot or shifted to a lower wavenumber indicating a possible split between α-helix and β-turn and/or intermolecular antiparallel β-sheet aggregates.

Deconvolution results were consistent among all myoglobin films, **Figures 2.11 & 2.12**. Deconvolution and curve fitting of the average spectra taken from a single film is shown in **Figure 2.13** (a. shows results of film before heating while b. shows results post heating). It is obvious that in the non-heated spectrum is dominated by the α-helix secondary structure at approximately 1653 cm^{-1}, while that of the β-sheet structure, 1630 cm^{-1}, and random coil/turns, 1677 cm^{-1}, are less prominent. After heating, however, the α-helix does not completely diminish, but the area ratio of α-helix to β-sheet decreases from approximately 3.00 to 1.75, indicative of significant β-sheet formation. At higher frequencies, after heating the random coil/turn peak at 1677 cm^{-1} was replaced with the 1686 cm^{-1} curve more prominent that the residual α-helix. The shift in the higher wavenumber, 1686 cm^{-1}, is likely indicative that intermolecular antiparallel β-sheet structure is formed upon heating. The average results plotted in **Figures 2.11 & 2.12** show that results are consistent with every myoglobin film. Heating decreases the ratio of α-helix to β-sheet secondary structure in parallel to that of all other protein secondary structures.

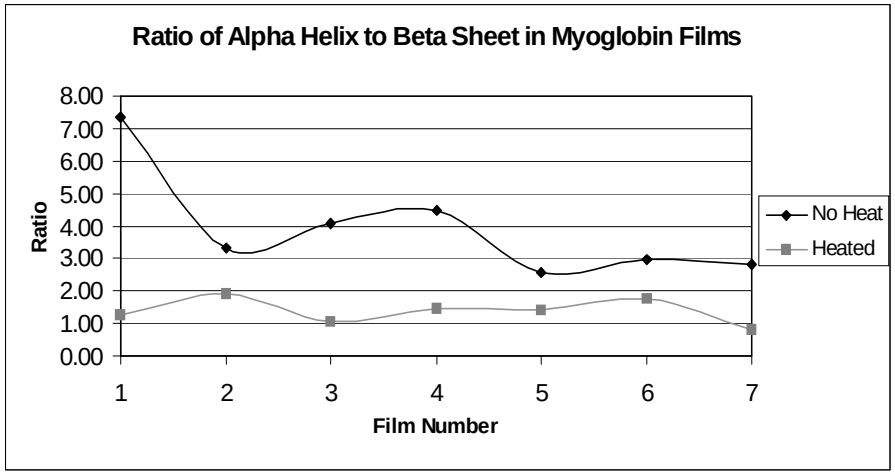

Figure 2.11: The amide I region of each of seven myoglobin film averages was deconvolved and modeled. Ratios of the areas of α-helix and β-sheet curves fit within this model are plotted above to show the difference in ratio between heated and unheated spectra.

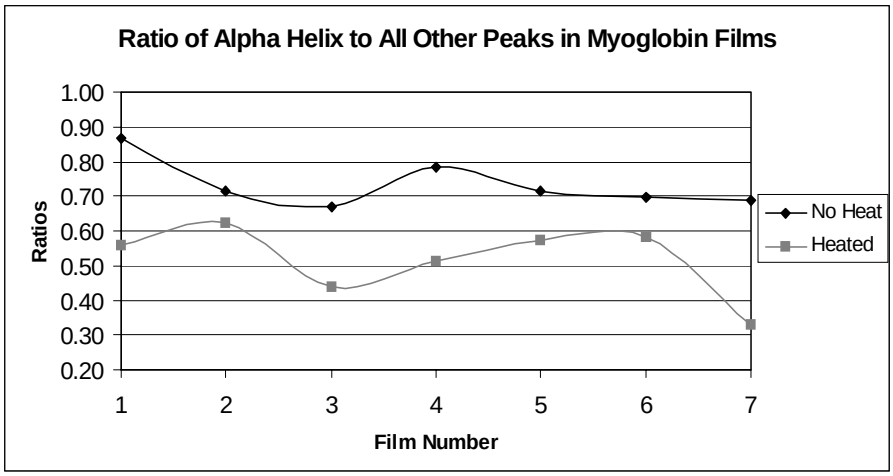

Figure 2.12: The amide I band of seven myoglobin peak averages was deconvolved and modeled. The ratios of the peak areas of the α-helix to all other curves fit within this model are plotted above to show that when the films are heated the amount of α-helix decreases.

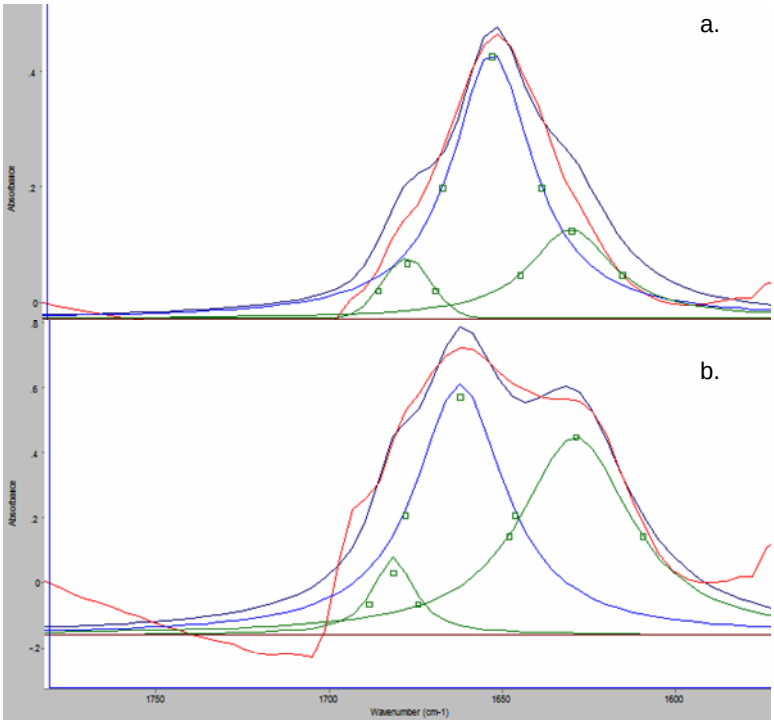

Figure 2.13: Spectra of protein secondary structure components contributing to the amide I band are modeled from average spectra of myoglobin films before heating (a) and after heating (b). The dark blue lines are deconvolved spectra. The red spectra are mathematical composites of the modeled components. Blue and green models were fit into the deconvolved spectra representing different secondary structures. Notice how the single component model located at approximately 1655 cm^{-1} representing α-helix is the most prominent in the unheated spectrum (a), but diminishes compared to other secondary structure curves that appear after heating (b).

To summarize the effects of the model protein studied, the location of 140 amide I peaks have been plotted for unheated protein films, heated protein films, and heated protein films' shoulder locations, **Figure 2.14**. The very slight deviation in the location of the peak maxima before heating indicates the homogeneity of the films. After heating the new peak maxima consistently shifts away from the depleted original peak to a higher or lower wavenumber, in approximately equal number. The shoulders stay in the original peak location or shift only slightly. Deconvolution of the amide I region from averaged spectra show that the area of α-helix decreases at the expense of β-sheet and other protein secondary structures upon heating.

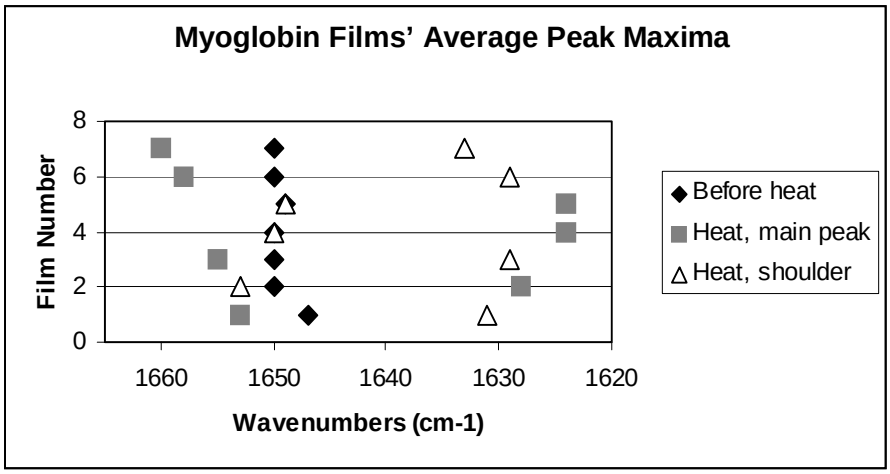

Figure 2.14: Frequency of the amide I peak maxima of the average spectra taken from seven myoglobin films before (black diamonds) and after (grey squares) heating plotted with the peak location of the shoulder (open triangles) found in spectra after heating. Before heating the black diamonds are in a relatively strait line along 1650 cm^{-1} representing homogeneity.

Application of the Proposed Method

Gelatin: After demonstrating feasibility with the model protein myoglobin to study the effects of thermal processing on protein secondary structure of the same film before and after heating, the method developed was applied to another protein from an animal source, gelatin. The amide I band of gelatin before heating, **Figure 2.15a**, showed a similar pattern as seen in myoglobin, the distribution is fairly tight. There are, however, only a few peaks that appear at higher wavenumbers, while the majority fall around 1636 cm^{-1}. Twenty spectra and corresponding spectral average from a single gelatin film are overlaid in **Figure 2.16**. Notice that there is little variation in the peak maxima location of approximately 1635 cm^{-1} for the twenty spectra and average, representing high homogeneity before heating.

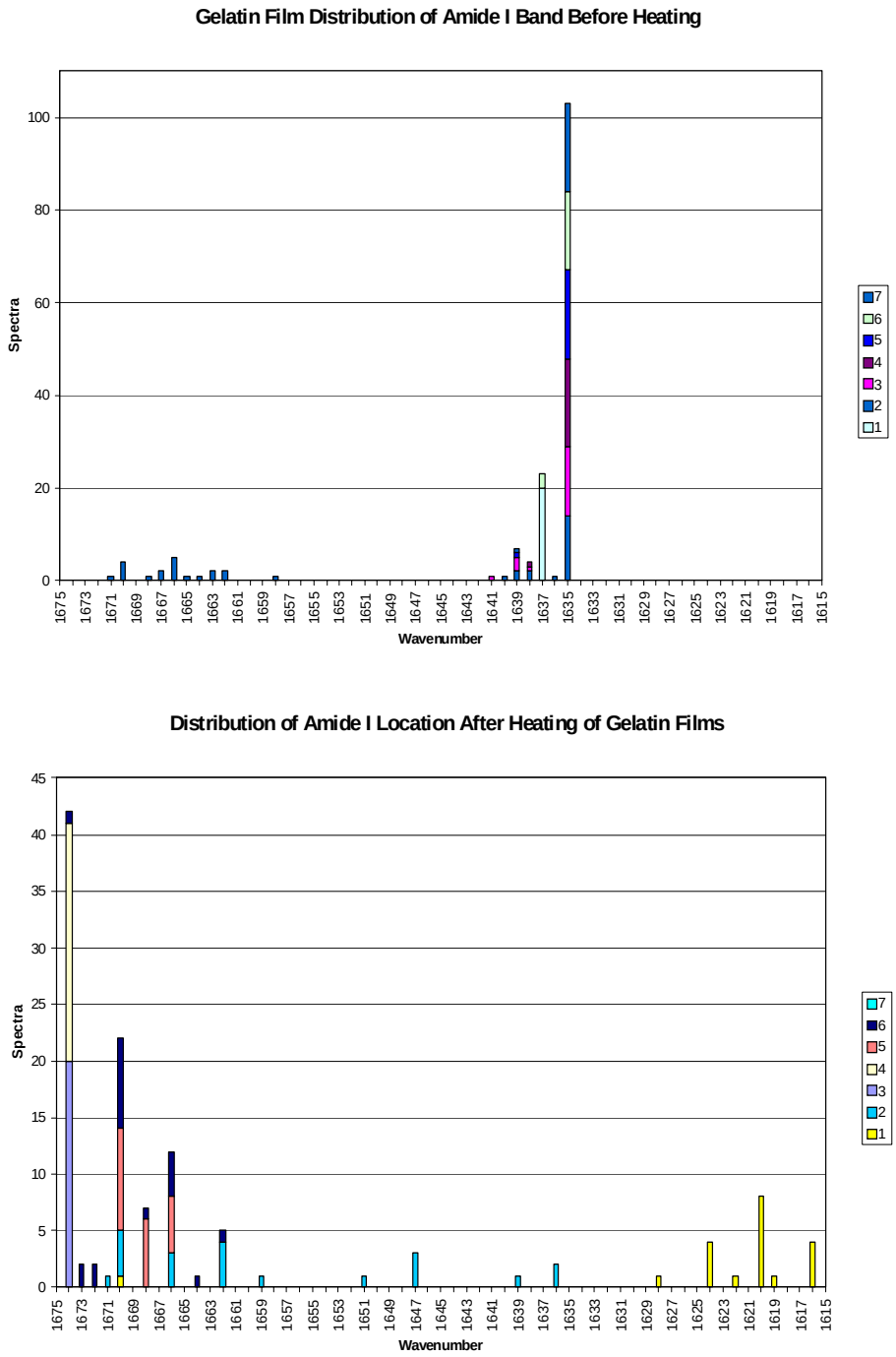

Figure 2.15: The amide I peak maxima plotted from 140 spectra from seven gelatin films before heating (top) and after heating (bottom).

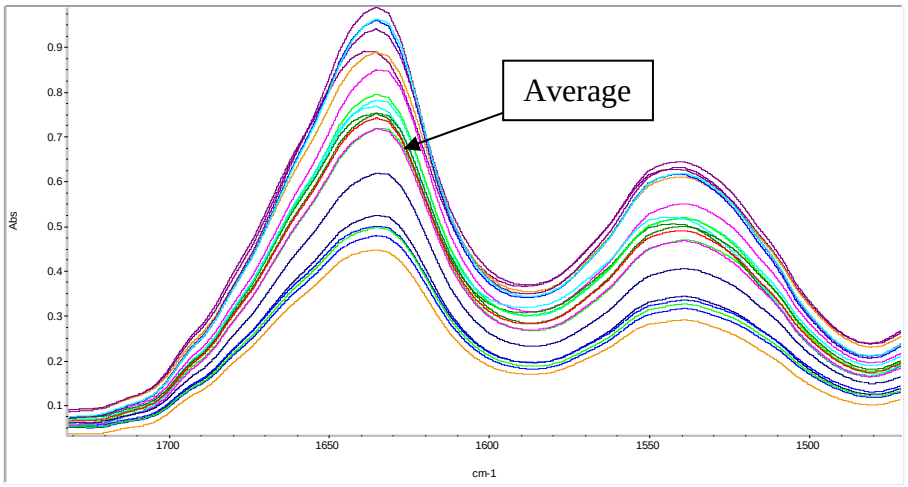

Figure 2.16: The amide region of twenty spectra and average (red) from a single gelatin film before heating in common view. The location of the peak maxima is approximately the same for all spectra.

The commercial manufacturing of gelatin involves an extended harsh acid or alkaline treatment of collagen followed by extraction between 55 and 100 ˚C and isolation of desired form. Highest quality gelatins are the first extracted at lower temperatures. With each successive extraction the quality of gelatin decreases and the extraction temperature increases **(88)**. Collagen exists in a triple helix conformation. Upon heating, gelatin takes on a random coil conformation, but while cooling attempts to rewind into the native triple helix form. Since gelatin has already been submitted to higher temperatures upon extraction it is possible that complete drying causes the gelatin to exist in a β-sheet conformation. Another possibility is a report in the range of 1640-1648 cm^{-1} as disordered structures **(24)** while the wavenumber range for disordered structures reported in another review **(27)** is slightly higher, 1642-1657 cm^{-1}. After heating the film and compiling the amide I peak maxima, **Figure 2.15b**, six of the seven films had shifts of the amide I band to higher wavenumbers, greater than 1660 cm^{-1}. The same band of the remaining film shifted to a lower wavenumber, 1620 cm^{-1}. This was interesting because it has been reported that **(74a)**, upon cooling, gelatin "renatures" and winds around neighboring molecules to form a combination of random coils and α-helices. It is possible that since the temperature is much higher than the denaturation temperature of the protein, more random coils and intermolecular antiparallel β-sheets form. **Figure 2.17** confirms the shift from lower to higher wavenumbers, with one film being the only exception, upon heating. In addition to the scatter plot, the spectra of all seven films' spectral averages before and after heating were plotted in full scale view, see **Figure 2.18**. This illustrates that all seven averages before heating

were essentially superimposed indicating homogeneity, but after heating there was a drastic shift to higher wavenumbers. Previous studies **(74)** of gelatin in solution showed that the native gelatin's amide I peak location falls around 1643 cm^{-1}. Upon heating, the peak shifted to lower wavenumbers, about 1633 cm^{-1}. This does not correlate well with the majority of the results from the present study. A significant difference in these earlier studies was that the gelatin is heated to a mere 50 ˚C in prior processing **(74)**, but a temperature of 100 ˚C was used in the present.

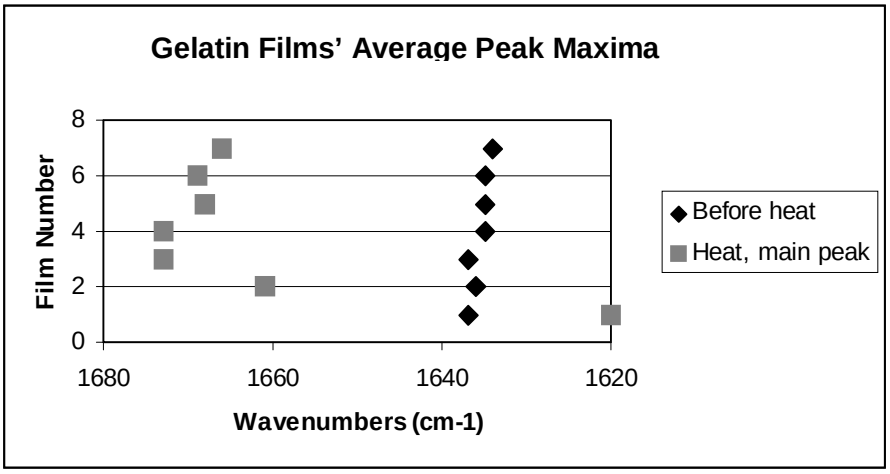

Figure 2.17: The frequency of the amide I peak maxima taken from gelatin film spectral averages before (black diamonds) and after (grey squares) heating. Gelatin is homogenous before heating.

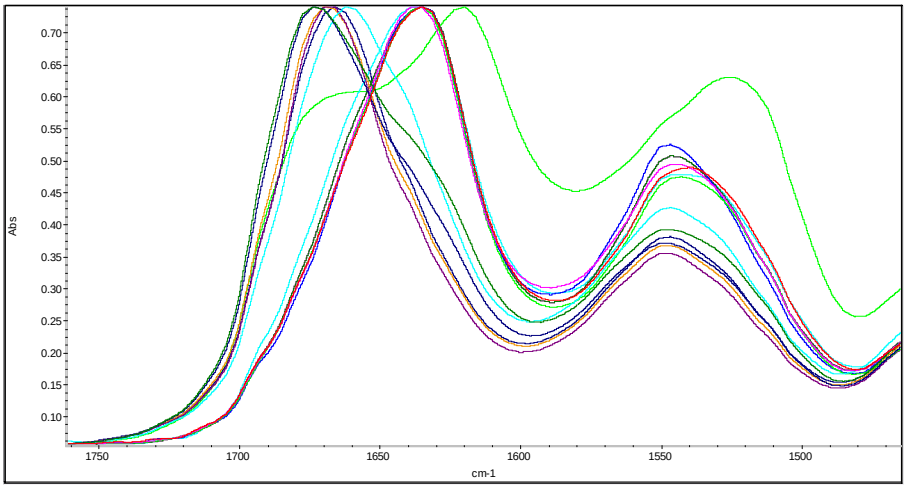

Figure 2.18: Spectral averages taken from seven films before and after heating. The eight spectra centered at approximately 1635 cm^{-1} are those taken from films before heating, while those shifted to higher or lower wavenumbers are those taken from films after heating.

The ratio of β-sheet content to that of the random coil/intermolecular antiparallel β-sheet, in deconvolved, modeled spectra, consistently decreases (**Figure 2.19)**. It can be noted that upon heating, there is an increase in the amount of random coil and/or intermolecular antiparallel β-sheet. The ratio of α-helix to β-sheet secondary structure was not consistent among the seven films. The results are spread about 50:50 (**Figure 2.20)**. **Figure 2.21** shows the deconvolved, curve fit, spectra of film four to illustrate this fact.

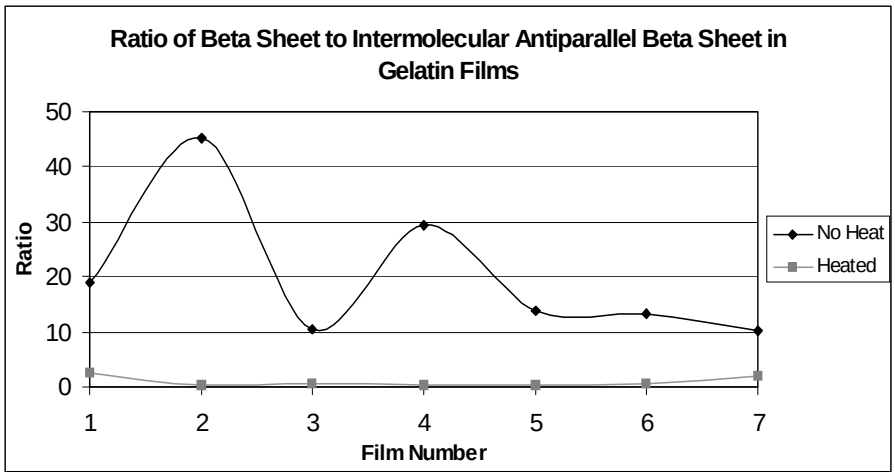

Figure 2.19: Area ratios taken from models fit into deconvolved amide I regions of seven gelatin film spectral averages are shown above. The amount of β-sheet deplinishes while that of the intermolecular antiparallel β-sheet increases upon heating.

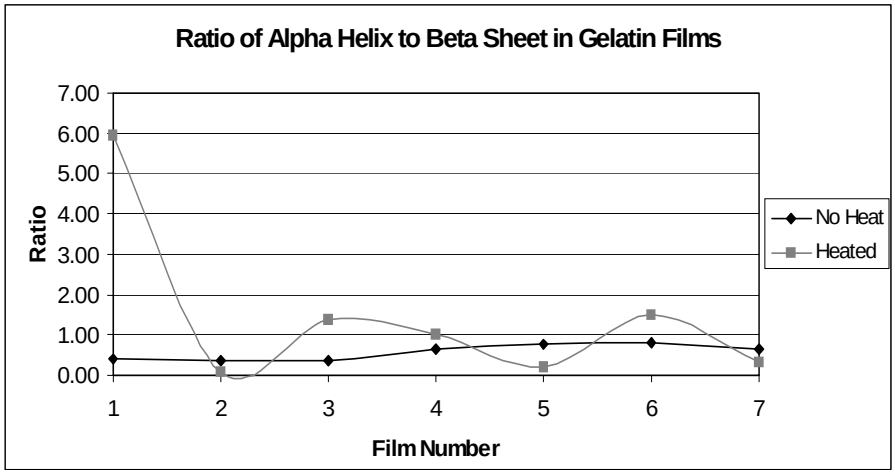

Figure 2.20: The amide I region of seven gelatin film spectral averages were deconvolved and modeled. Area ratios from models representing α-helix and β-sheet were plotted above.

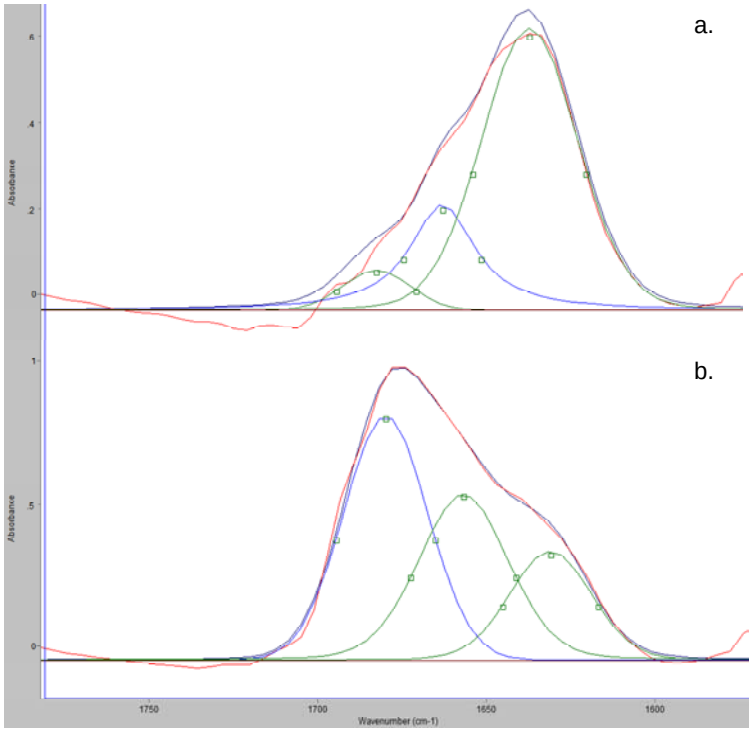

Figure 2.21: Spectra of protein secondary structure components contributing to the amide I band are modeled from average spectra of gelatin films before heating (a) and after heating (b). The dark blue lines are deconvolved spectra. The red spectra are mathematical composites of the modeled components. Blue and green models were fit into the deconvolved spectra representing different secondary structures. Notice how the model located at approximately 1635 cm^{-1} representing β-sheet secondary structure is the most prominent in the unheated spectrum (a), but diminishes compared to that of intermolecular antiparallel β-sheet at approximately 1680 cm^{-1} (b).

Wheat Gluten: WG, the plant source, results are more unusual than that of myoglobin and gelatin. **Figure 2.22** shows the same results for WG that are seen in both the myoglobin and gelatin films before heating occurs; the location of the amide I peak before heating is relatively homogeneous. For all 21 spectra shown the frequency of the amide I peak is approximately 1647 cm^{-1}. After heating, however, the peaks shift to higher wavenumbers (**Figure 2.23)**. This does not correlate with previous studies, showing a shift to lower wavenumbers in gliadin films dried at 70 ˚C, **(66),** and solubilized gluten heated to 85 ˚C **(65)**. As with the differences seen between prior and present studies of gelatin, the prior wheat gliadin and gluten studies were performed at lower temperatures. Deconvolved, fit curves were ratioed in various ways shown in **Table 2.1**. There is no consistency among the results for films one through three that were prepared in the same way. The distribution of the amide I peak location does broaden after heating, **Figure 2.24**. This is indicative of secondary structure change.

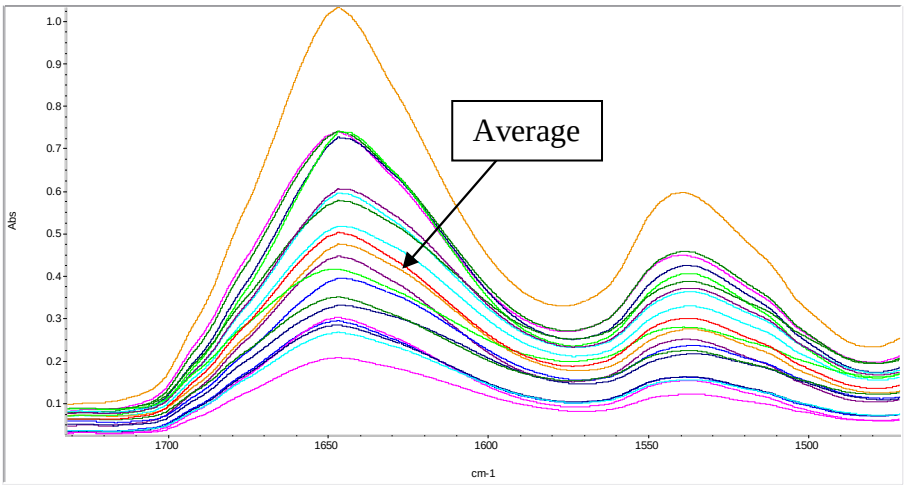

Figure 2.22: The amide region of twenty spectra and average (red) from a single wheat gluten film before heating in common view. The location of the peak maxima, 1647 cm^{-1}, is approximately the same for all spectra.

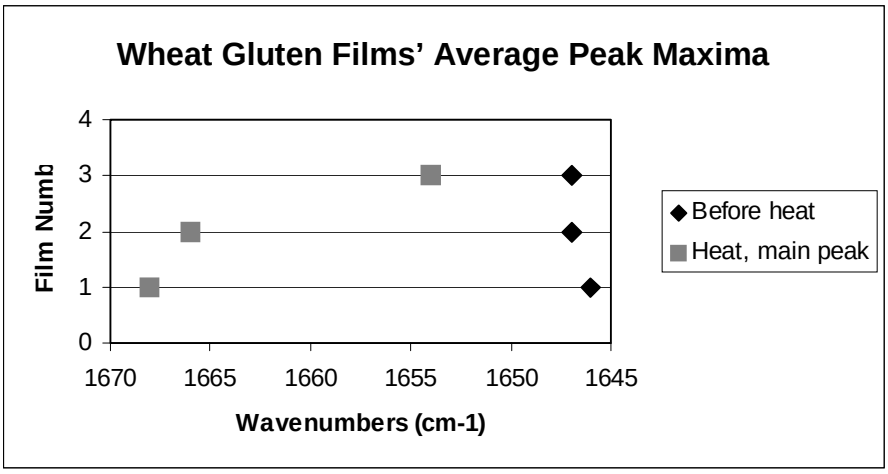

Figure 2.23: Frequency of amide I peak maxima taken from three wheat gluten films before (black diamonds) and after (grey squares) heating.

Table 2.1: Deconvolution Results from Wheat Gluten

Alpha Helix to Beta Sheet			
Film Number	1	2	3
No Heat	1.07	2.70	1.83
Heated	0.53	3.82	1.31
Alpha Helix to all others			
Film Number	1	2	3
No Heat	0.32	0.56	0.45
Heated	0.16	0.79	0.52
Alpha Helix to Intermolecular Beta Sheet			
Film Number	1	2	3
No Heat	1.38	5.31	3.16
Heated	0.30	67.86	6.44

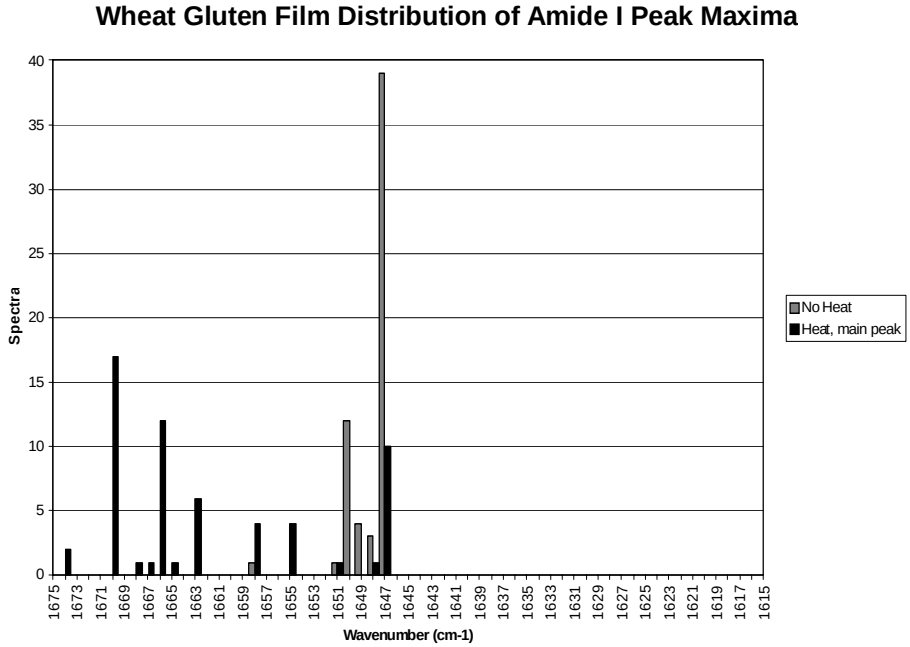

Figure 2.24: The amide I peak maxima taken from 60 spectra of three films before heating (solid) and 60 spectra of three films after heating (shaded).

Two films were cast from WG that had been ground with a mortar and pestle before extraction. **Figure 2.25** shows the frequency of the amide I peak maxima for these. In both of these cases the initial amide I location was slightly higher than the films that had not been ground with mortar and pestle (shown in **Figure 2.23**), and after heating the amide I peak location dropped only slightly. Previous studies on hydrated wheat gluten proteins in their solid state **(88b)** reveal that the amount of α-helix and β-turn increase relative to β-sheet upon the hydration of gluten proteins. This suggests a possible explanation for the higher amide I location in these two films. If additional wheat gluten is solubilized, it is speculated that the heat treatment could have less severe of an effect.

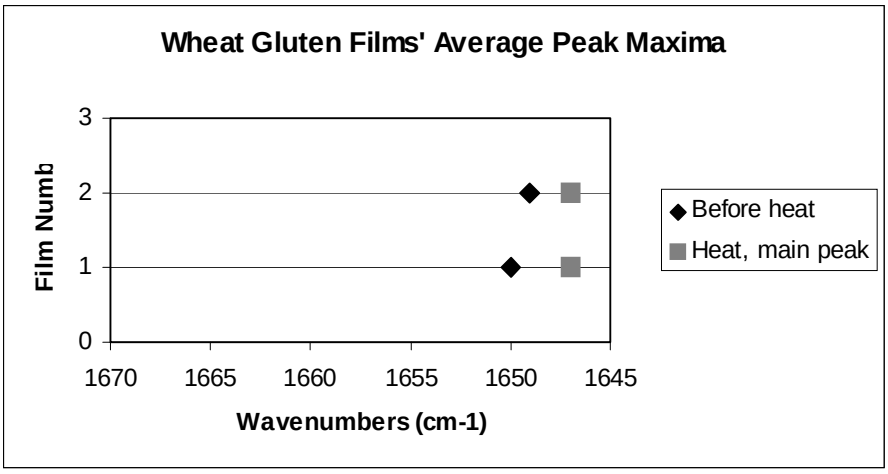

Figure 2.25: Frequency of the amide I peak maxima taken from wheat gluten films cast from wheat gluten ground with a mortar and pestle before extraction.

An additional two films were cast from WG that followed the same extraction procedure as the first three films discussed, but with a total extraction time of 30 min instead of 2 min. The location of the amide I peak before and after heating for these films is shown in **Figure 2.26**. Film one shows a similar frequency location before heating as the first three films. After heating, however, the peak location shifted to a lower frequency. The second film resulted in the highest amide I peak frequency seen among all WG films, which could possibly be a result of more gluten hydration, discussed above. After heating, there was no change in peak location; therefore, two points are not visible in **Figure 2.26**.

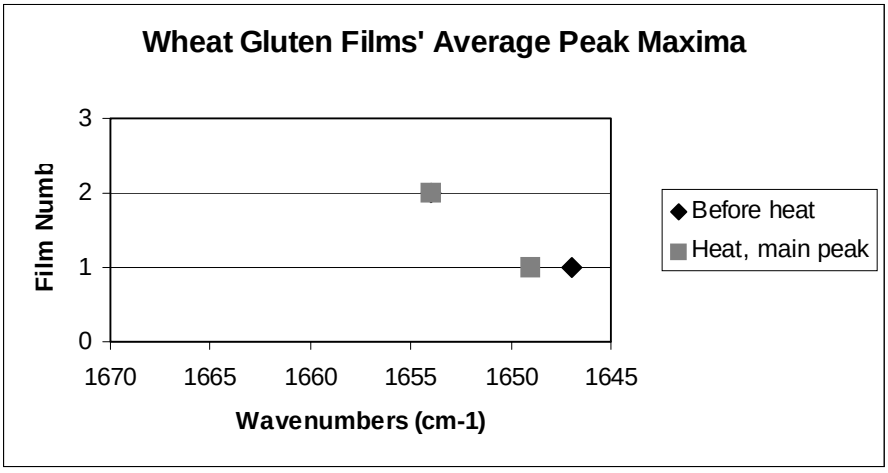

Figure 2.26: Frequency of the amide I peak maxima taken from wheat gluten films cast from wheat extracted for an extended time. The location of the amide I peak in film 2 is approximately equal before and after heating; therefore, the black diamond from film 2, before heating, is not visible.

There is considerable variation among the results seen in WG versus those in myoglobin or gelatin. Previous studies have shown that the effects of heating are reversible to an extent. It is possible that the amount of heating on both gelatin and myoglobin were so intense that the protein was unable to fold back into its α-helical conformation similar to WG. Denaturation temperature of myoglobin at various pH levels all fall below 100 ˚C (**89)**. Gelatin denatures at a much lower temperature, 40 ˚C **(90)**. A study on the determination of denaturation temperatures of various wheat proteins states that for gluten proteins there are two denaturation temperatures, 64 and 84 ˚C **(91)**. In the introduction for the same article it also states that previous studies have reported denaturation temperatures for gluten up to 112 ˚C. It is interesting to note that the maximum amount of change occurred in the protein, gelatin, which had the lowest denaturation temperature, followed by myoglobin and WG. Since one of the denaturation temperatures of WG falls around 100 ˚C it is not ludicrous that there was not as dramatic of a difference in the WG as compared to other raw materials tested. The unexpected increase in α-helical content seen in the majority of the films could be due to this fact, but is pure speculation by the author.

A previous thermal heating study on wheat gluten **(65)** states that formation of β-sheet is reversible upon cooling, but less reversible upon heating above 45 ˚C. If the denaturation temperature is higher than 100 ˚C, it is possible that the secondary structure, upon cooling, over compensated the reversal with additional α-helix formation. All assumptions made in the previous paragraph are purely speculative.

In summary, the use of stainless steel as a reflective substrate to study the changes in protein secondary structure during thermal processing in warranted. The use of this inexpensive, relatively rapid method permits the study of the exact location on protein films before and after heating. Overall, before heating the distribution of the amide I peak location within the center of the film is relatively compact. After heating, in most cases, the distribution spreads out. Peaks and side lobes occurring around 1620 and 1685 cm^{-1} have been documented as intermolecular antiparallel β-sheets and are a common sign of aggregation. With the method options are available to study the effects of varying temperatures and times of heating of the film. Implication for food processing techniques including extrusion, pasteurization and spray drying may prove to be valid in the future.

In summary, the use of stainless steel as a reflective substrate to study the changes in protein secondary structure during thermal processing in warranted. The use of this inexpensive,

relatively rapid method permits the study of the exact location on protein films before and after heating. Overall, before heating the distribution of the amide I peak location within the center of the film is relatively compact. After heating, in most cases, the distribution spreads out. Peaks and side lobes occurring around 1620 and 1685 cm^{-1} have been documented as intermolecular antiparallel β-sheets and are a common sign of aggregation. With the method options are available to study the effects of varying temperatures and times of heating of the film. Implication for food processing techniques including extrusion, pasteurization and spray drying may prove to be valid in the future.

Advantages offered by this microspectroscopic imaging method include the ability of revealing homogeneity or heterogeneity with spectra for 20 contiguous pixels not offered using macro techniques. Thermal processing on an ATR crystal is impossible. Casting of the film using a small diameter needle on polished stainless steel, on the other hand, allows spectroscopic examination of the entire film before and after heating. Point probing, as done with ATR, is unreliable because of its dependence on a few specific targeted areas, while imaging allows the entire area to be characterized and the selection of multiple spectra within the film.

References

1. Symes, K.J. 1965. The inheritance of grain hardness in wheat as measure by the particle size index. *Aust. J. Agric. Res*. 16 (2): 113-123.

2. Simmonds, D. H., Barlow, K. K., and Wrigley, C. W. 1973. The biochemical basis of grain hardness in wheat. *Cereal Chem*. 50:553-562.

3. Barlow, K. K., Buttrose, M. S., Simmonds, D. H., and Vesk, M. 1973. The nature of the starch-protein interface in wheat endosperm. *Cereal Chem*. 50:443-454.

4. Mattern, P.J., Morris. R. Schmidt, J.W. and Johnson, V.A. 1973. Location of genes for kernel properties in the wheat cultivar "Cheyenne" using chromosome substitution lines. In: *Proceedings of the 4th International Wheat Genetics Symposium*. E.R. Sears and L.M.S. Sears (Eds.), University of Missouri, Colombia, MO. Pgs 703-707.

5. Greenwell, P., and Schofield, J.D. 1986. What makes hard wheats soft?. *FMBRA Bulletin*. 4: 139-149.

6. Blochet, e-E., Chevalier, C., Forest, E., Pebay-Peyroula, E., Gautier, M-F, Joudrier, P., Pézolet, M. and Marion, D. 1993. Complete amino acid sequence of puroindoline, a new basic and cystine-rich protein with a unique tryptophan-rich domain, isolated from wheat endosperm by Triton X-114 phase partitioning. *FEBS Letters*. 30(3): 336-340.

7. Giroux, M.J., and Morris, C.F. 1997. A glycine to serine change in Puroindoline b is associated with wheat grain hardness and low levels of starch-surface Friabilin. *TAG Theor. Appl. Genet*. 95 (5-6) 857-864.

8. Morris, C.F. 2002. Puroindolines: the molecular genetic basis of wheat grain hardness. *Plant Mol. Biol.* 48: 633-647.

9. Turnbull, K.-M. and Rahman, S. 2002. Endosperm texture in wheat. *J. Cereal Sci.* 36:327-337.

10. Anjum, F. M., and Walker, C. E. 2006. Review on the significance of starch and protein to wheat kernel hardness. *J. Sci. Food. Agr*. 56 (1) 1-13.

11. Piot, O., Manfait, M. and Autran, J.C. 1999. Spatial distribution of protein and phenolics in wheat grain as probed by confocal Raman spectral imaging. *AACC Conf. Abstracts.* O129.

12. Piot, O. Autran, J.C. and Manfait, M. 2000. Molecular bases of kernel hardness as probed by confocal Raman microspectroscopy: An investigation on the role of endosperm cell walls. *AACC Conf. Abstracts.* O341.

13. Piot, O. Autran, J.C. and Manfait, M. 2002. Assessment of cereal quality by micro-raman analysis of the grain molecular composition. *Appl. Spectrosc*. 56: 1132-1138.

14. Piot, O., Autran, J.-C. and Manfait, M. 2000. Spatial distribution of protein and phenolic constituents in wheat grain as probed by confocal Raman microspectroscopy. *J. Cereal Sci.* 32:57-71.

15. Piot, O., Autran, J.-C., Manfait, M. 2001. Investigation by confocal Raman microspectroscopy of the molecular factors responsible for grain cohesion in the *Triticum aestivum* bread wheat. Roll of the cell walls in the starchy endosperm. *J. Cereal Sci.* 34:191-205.

16. Wetzel, D.L., Srivarin, R. and Finney, J.R. 2003. Revealing protein infrared spectral detail in a heterogeneous matrix dominated by starch. *Vib. Spectros*. 31, 109-114.

17. Mihalyi, E. 1978. *Application of proteolytic enzymes to protein structure studies*. E. Mihalyi (ed.). CRC Press. West Palm Beach, FL.

18. 2005. Proteins: three-dimensional structure. In: *Fundamentals of biochemistry: life of the molecular level*. D. Voet, J.G. Voet, and C.W. Pratt (eds.). Jon Wiley & Sons, Inc. Hoboken, NJ. pgs. 129-180.

19. 1994.*Structure-function properties of food protein*. L. Phillips, D.M. Whitehead, and J. Kinsella (eds.) Academic Press. San Diego, CA.

20. Ludescher, R.D. 1996. Physical and chemical properties of amino acids and proteins. In: *Food Proteins: Properties and Characterization*. S. Nakai and H.W. Modler (eds.), Wiley-VCH. New York, NY. Pgs 23-68.

21. Boyes-Watson, J., Davidson, E. and Perutz, M.F. 1949. An X-ray study of horse methaemoglobin. *Proc. Roy. Soc. A.* 191(1024): 83-132.

22. Green, D.W., Ingram, V.M. and Perutz, M.F. 1954. The Structure of Haemoglobin. IV. Sign Determination by the Isomorphous Replacement Method. *Proc. Roy. Soc. A.* 225(1162): 287-307.

23. Kendrow, J.C. and Parrish, R.G. 1956. The crystal structure of myoglobin III: sperm-whale myoglobin. *Proc. Roy. Soc. A*. 238(1214): 305-324.

24. Jackson, M. and Mantsch, H.H. 1995. The use and misuse of FTIR spectroscopy in the determination of protein structure. *Crit. Rev. Biochem. Mol. Biol.* 30(2): 95-120.

25. 2005. Infrared spectroscopy. In: *Undergraduate Instrumental Analysis-6th edition*. J.W. Robinson, E.M.S. Frame and G.M. Frame II (eds.). Marcel Dekker. New York, NY. Pgs 213-310.

26. Elliot, A. and Ambrose, E.J. 1950. Structure of synthetic polypeptides. *Nature*. 165. 921-922.

27. Barth, A. and Zscherp, C. 2002. What vibrations tell about proteins. *Q. Rev. Biophys*. 35: 369-430.

28. Abe, Y. and Krimm, S. 1972. Normal vibrations of crystalline polyglycine I. *Biopolymers*. 11: 1817-1839.

29. Miyazawa, T. 1960. Perturbation Treatment of the Characteristic Vibrations of Polypeptide Chains in Various Configurations. *J. Chem. Phys.* 32: 1647-1652.

30. Krimm, S. and Bandekar, J. 1986. Vibrational spectroscopy and conformation of peptides, polypeptides, and proteins. *Adv. Protein Chem.* 38: 181-364.

31. Chirgadze, Y.N., Fedorow, O.V., and Trushina, N.P. 1975. Estimation of amino acid residue side chain absorptions in the infrared spectra of protein solutions in heavy water. *Biopolymers.* 14: 679-694.

32. Venyaminov, S.Y. and Kalnin, N.N. 1990. Quantitative IR spectrophotometry of peptide compounds in water (H_2O) solutions. I. Spectral parameters of amino acid residue absorption bands. *Biopolymers*. 30: 1243-1257.

33. Wetzel, D.L. 1995. Microbeam molecular spectroscopy of biological materials. In: *Food Flavors: Generation, Analysis and Process Influence.* G. Charalambous (ed.), Elsevier. Pgs 2039-2108.

34. Choo, L.P., Wetzel D.L., Halliday, W.C., Jackson, M., LeVine, S.M. and Mantsch, H.H. 1996. *In situ* characterization of beta-amyloid in Alzheimer's diseased tissue by synchrotron Fourier transform infrared microspectroscopy. *Biophys. J.* 71. 1672-1679.

35. Schweitzer-Stenner, R. 2006. Advances in vibrational spectroscopy as a sensitive probe of peptide and protein structure: A critical review. *Vib. Spectros.* 42: 98-117.

36. Haris, P.I. and Chapman, D. 1992. Does Fourier-transform infrared spectroscopy provide useful information on protein structures?. *Trends Biochem Sci.* 17(9):328-333.

37. Haris, P.I. and Severcan, F. 1999. FTIR spectroscopic characterization of protein structure in aqueous and non-aqueous media. *J. Mol. Catal. B: Enzymatic*. 7: 201-221.

38. Bruun, S.W., Søndergaard, I. and Jacobsen, S. 2007. Analysis of protein structures and interactions in complex food by near-infrared spectroscopy. 1. gluten powder. *J. Agric. Food Chem.* 55: 7234-7243.

39. Bruun, S.W., Sondergaard, I. and Jacobsen, S. 2007. Analysis of protein structures and interactions in complex food by near-infrared spectroscopy. 2. Hydrated gluten. *J. Agric. Food Chem*. 55(18): 7244-7251.

40. Mo, C., Peiyi, W., Chen, X. and Shao, Z. 2006. Near-infrared characterization on the secondary structure of regenerated *Bombyx mori* silk fibroin. *Appl. Spectros.* 60(12): 1438-1441.

41. Arseniev, A.S., Kondakov, V.I., Maiorov, V.N. and Bystrov, V.F. 1984. NMR solution spatial structure of 'short' scorpion insectotoxin I_5A. *FEBS Letters.* 165(1): 57-62.

42. Braun, W., Bösch, C., Brown, L.R., Gō, N. and Wüthrich, K. 1981. Combined use of proton-proton overhauser enhancements and a distance geometry algorithm for determination of polypeptide conformations. Application to micelle-bound glucagons. *Biochem. Biophys. Acta.* 667(2): 377-396.

43. Güntert, P. 1998. Structure calculation of biological macromolecules from NMR data. *Q. Phys. Rev.* 31(2): 145-237.

44. Cavanagh, J., Fairbrother, W.J., Palmer III, A.G., Rance, M. and Skelton, N.J. 2007. *Protein NMR Spectroscopy.* Elsevier Inc. Burlington, MA.

45. Chou, P.Y. and Fasman, G.D. 1974. Conformational parameters for amino acids in helical, β-sheet, and random coil regions calculated from proteins. *Biochemistry*. 13(2): 211-222.

46. Chou, P.Y. and Fasman, G.D. 1974. Prediction of protein conformation. *Biochemistry*. 13(2): 222-245.

47. Taylor, J.W., Bayles, B.B., and Fifield, C.C. 1939. A simple measure of kernel hardness in wheat. *Am. Soc. Agron*. 31: 775-784.

48. American Association of Cereal Chemists. 2000. Particle size index for wheat. In: Approved Methods of the American Association of Cereal Chemists, 10th ed. Methods 55-30, 55-31 and 39-70A. The Association: St. Paul, MN.

49. Culter, G.H. and Brinson, G.A. 1935. The granulation of whole wheat meal and a method of expressing it numerically. *Cereal Chem*. 12: 120-129.

50. Williams, P.C. and Sobering, D.C. 1986. Attempts at standardization of hardness testing of wheat. I. the grinding/sieving (particle size index) method. *Cereal Foods World.* 31: 359-364.

51. Wetzel, D.L., Williams, P.C. and Mark, H. 1978. NIR flour QC. AACC Conf. Abstracts, *Cereal Foods World.* 24.

52. Mattern, P.J. 1988. Wheat hardness: a microscopic classification of individual grains. Cereal Chem. 65(4): 312-315.

53. Massie, D.R., Slaughter, D.C., Abbott, J.A. and Hruschka, W.R. 1993. Acoustic single-kernel wheat hardness. *Trans. ASAE*. 36: 1393-1398.

54. Eilert, A. 1986. Acousto-optic tunable filter spectroscopic instrumentation for quantitative near-IR analysis of organic materials. Thesis.

55. Roberts, H.F. 1910. A quantitative method for the determination of hardness in wheat. *Kans. Agr. Expt. Sta. Bul.* 167: 371-390.

56. Gaines, C.S., Finney, P.F., Fleege, L.M. and Andreww, L.C. 1996. Predicting hardness measurement using the single kernel characterization system. *Cereal Chem.* 72(2): 278-283.

57. Eckhoff, S.R., Supak, W.A. and Davis, A.B. 1988. A rapid single-kernal wheat hardness tester. *Cereal Chem.* 65(6):503-508.

58. Mills, E.N.C., Parker, M.L., Wellner, N., Toole, G., Feeney, K., Shewry, P.R. 2005. Chemical imaging: the distribution of ions and molecules in developing and mature wheat grain. *J. Cereal Sci.* 41: 193-201.

59. Reffner, J., Carr, G.L., Sutton, S., Hemley, R.J. and Williams G.P. 1994. Infrared microspectroscopy at the NSLS. *Sync. Rad. News.* 7(2): 30-37.

60. Miller, L.M. and Dumas, P. 2006. Chemical imaging of biological tissue with synchrotron infrared light. *Biochim. Biophys. Acta.* 1758, 846-857.

61. Wetzel, D.L. 2007. Biomedical applications of infrared microspectroscopy and imaging by various means. In: *Modern Concepts in Biomedical Infrared Microspectroscopy.* P. Lasch and J. Kniepp (eds). Blackwell, Oxford. (in press)

62. 2001. Spectrum Spotlight User's Guide. Perkin Elmer Instruments. Page 17.

63. 2005. *Spectrochemical analysis using infrared multichannel detectors.* R. Bhargava and I.W. Levin. Blackwell Pub. Ames, IA.

64. Byler, D.M., and Susi, H. 1986, Examination of the Secondary structure of proteins by deconvolved FTIR spectra. *Biopolymers*, 25, 469-487.

65. Georget, D.M.R and Belton, P.S. 2006. Effects of temperature and water content on the secondary structure of wheat gluten studied by FTIR spectroscopy. *Biomacromolecules.* 7: 469-475.

66. Mangavel, C., Barbot, J., Papineau, Y. and Guéguen, J. 2001. Evolution of wheat gliadins conformation during film formation: a fourier transform infrared study. *J. Agric. Food Chem.* 49: 867-872.

67. Bihan, T.L., Blochet, J.-E., Désormeaux, A., Marion, D., and Pézolet, M. 1996. Determination of the secondary structure and conformation of puroindolines by infrared and Raman spectroscopy. *Biochemistry.* 35: 12712-12722.

68. Igrejas, G. Gaborit, T., Oury, F-X., Chiron, H., Marian, D., and Banlard, G. 2001. Genetic and environmental effects on puroindoline-a and puroindoline-b content and their relationship to technological properties in French wheat bread. *J. Cereal Sci.* 34(1) 37-47.

69. Panozzo, J. F. and Eagles, H. A. 2000. Cultivar and environmental effects on quality characters in wheat. II. Protein. *Aust. J. Agr. Res.* 51(5) 629-636.

70. Doehlert, D.C. and McMullen, M.S. 2000. Genotypic and environmental effects on oat milling characteristics and groat hardness. *Cereal Chem*. 77(2) 148-154.

71. Ambrose, E.J. and Elliott, A. 1951. Infra-red spectroscopic studies of globular protein structure. *Proc. Roy. Soc.* 208A: 75-90.

72. Clark, A.H., Sauderson, D.H.P. and Suggett, A. 1981. Infrared and laser-Raman spectroscopic studies of thermally induced globular protein gels. *Int. J. Peptide and Protein Res.* 17:353-364.

73. Boye, J.I., Alli, I., Ismail, A.A., Gibbs, B.F. and Konishi, Y. 1994. Factors affecting molecular characteristics of whey protein gelation. *Int. Dairy J.* 5:337-353.

74a. Watenabe, K., Tezuka, Y., Tadahiro, Ishii, 1997. Configuration between re-formed collagen triple helices and artificially introduced cross-links in gelatin gels. *Macromolecules* 30, 7910-7913.

74. Payne, K.J. and Veis, A. 1988. Fourier transform IR spectroscopy of collagen and gelatin solutions: deconvolution of the amide I band for conformational studies. *Biopolymers*. 27: 1749-1760.

75. Lefévre, T. and Subirade, M. 1999. Structural and interaction properties of β-lactoglobulin as studied by FTIR spectroscopy. *Int. J. Food Sci. Tech.* 34: 419-428.

76. Byler, D.M. and Purcell, J.M. 1989. FTIR examination of thermal denaturation and gel formation in whey proteins. *SPIE, Fourier Transform Spec.* 1145: 415-417.

77. Meeserman, F., Smeller, L., and Heremans, K. 2002. Comparitive Fourier transform infrared spectroscopy study of cold-, pressure-, and heat-induced unfolding and aggregation of myoglobin. *Biophys. J.* 82: 2635-2644.

78. Elmore, D.L., Smith, S.A., Lendon, C.A. and Muroski, A.R. 2007. Probing the structural effects of pasteurization and spray drying on soy protein isolate in the presence of trehealose using FT-IR-ATR and FT-Raman spectroscopy. *Spectrosc.* 22(5):38-44.

79. Prudêncio-Ferreira, A.H. and Arêas, J.A.G. 1993. Protein-protein interactions in the extrusion of soya at various temperatures and moisture contents. *J. Food Sci.* 58(2): 378-384.

80. Jackson, M. and Mantsch, H. 1992. Artifacts associated with the determination of protein secondary structure by ATR-IR spectroscopy. *Appl. Spectros.* 46(4): 699-701.

81. Kretschmer, C.B. 1957. Infrared spectroscopy and optical rotatory dispersion of zein, wheat gluten and gliadin. *J. Phys. Chem.* 61(12):1627-1631.

82. Goormaghtigh, E., Cabiaux, V., and Ruysschaert, J-M. 1990. Secondary structure and dosage of soluble and membrane proteins by attenuated total reflectance Fourier transform infrared spectroscopy of hydrated films. *Eur. J. Biochem.* 193:409-420.

83. Subirade, M., Kelly, I., Guéguen, J. and Pézolet, M. 1998. Molecular basis of film formation from a soybean protein: comparison between conformation of glycinin in aqueous solution and in films. *Int. J. Biol. Macromol*. 23: 241-249.

84. Smeller, L., Rubens, P., and Heremans, K. 1999. Pressure effect on temperature-induced unfurling and tendency to aggregate of myoglobin. *Biochemistry*. 38:3816-3820.

85. Nabet, A. and Pézolet, M. 1997. Two-dimensional FT-IR spectroscopy: a powerful method to study the senconary structure of proteins using H-D exchange. *Appl. Spectros*. 51(5): 466-469.

86. Yang, W.J., Griffiths, P.R., Byler, D.M., and Susi, H. 1985. Protein conformation by infrared spectroscopy resolution enhancement by Fourier self-deconvolution. *Appl. Spectros.* 39 (2), 282-287.

87. Evans, S.V. and Brayer, G.D. 1990. High-resolution study of the three dimensional structure of horse heart metmyoglobin. *J. Mol. Biol.* 213: 885-897.

88. Ledward, D.A. 2000. Gelatin. In: *Handbook of Hydrocolloids*. G.O. Phillips and P.A. Williams (eds.). Woodhead Publishing Ltd. And CRC Press. Boca Raton, FL. Pgs: 67-86.

88b. Pézolet, M., Bonenfant, S., Dousseau, F., and Yves, Popineau. 1992. Conformation of wheat gluten proteins. *FEBS Letters.* 299(3): 247-250.

89. Hunt, M.C., Sørheim, O., and Slinde, E. 1999. Color and heat denaturation of myoglobin forms in ground beef. *J. Food Sci*. 64 (5): 847–851

90. Bigi, A., Panzavolta, S. and Rubini, K. 2004. Relationship between triple-helix content and mechanical properties of gelatin films. *Biomaterials*. 25(25): 5675-5680.

91. León, A., Rosell, C.M., and Benedito de Barver, C. 2003. A differential scanning calorimetry study of wheat proteins. *Eur. Food Res. Technol.* 217:13-16.

Abbreviations

American Association of Cereal Chemists	AACC
Attenuated Total Reflectance	ATR
Brookhaven National Laboratory	BNL
Focal Plane Array	FPA
Fourier Transform Infrared	FT-IR
Grain Softness Protein	GSP
Mercury Cadmium Telluride	MCT
National Synchrotron Light Source	NSLS
Near Infrared	NIR
Nuclear Magnetic Resonance	NMR
Single Kernel Classification System	SKCS
Transition Dipole Coupling	TDC
Vacuum Ultraviolet	VUV
Wheat Gluten	WG

Appendix A- Approaches to Relative Protein Secondary Structure

The following is a description of the learning process in determining a procedure for modified protein secondary structure subsequent calculations.

Wheat Endosperm Hardness Data

The procedure stated in the experimental section of Chapter 1 was the exact procedure used in the 2003 article "Revealing protein infrared spectral detail in a heterogeneous matrix dominated by starch" by Wetzel and coworkers **(A1)**. This procedure using GRAMS"RAZOR" software (ThermoGalactic, Salem, NH) was recommended to Wetzel by Dave Himmelsbach after working with typical data sets. This software was adopted in our laboratory and used to calculate secondary structure components for wheat specimens listed in the article. The main drawback is that each spectrum needs to be processed individually. For one wheat specimen, 20-25 spectra are selected, and processed one at a time. This means that for a given year with approximately 25 different wheat cultivars, greater than 625 spectra are individually processed. For routine application to assist the wheat breeding program, the time required for these calculations is immense.

Attempt to Apply Clustering

At the fall 2005 FACSS meeting, Wetzel discussed this dilemma with French physicist (University of Paris Sud), Paul Dumas, a synchrotron colleague of Wetzel and renowned microspectroscopist. Dumas suggested the use of clustering using ISys software. Dumas kindly worked with a typical data set that exemplified the protocol and results. The clustering approach involved grouping of all spectral data to filter out pixels dominated by starch and highlight proteinaceous pixels with similar secondary structure configuration. In theory, clustering results in a set of very similar spectra that could be accounted for by their average spectrum. Time and labor would be reduced with only one spectrum per wheat. This would reduce secondary structure determination from 625 calculations per year to 25.

The following summer, 2006, while mapping the 2005 crop year at NSLS, simultaneous attempts were made using clustering with ISys (Spectral Dimensions/Malvern, Columbia MD)

and Cytospec (www.cytospec.com/) software. Both clustering procedures involved a series of pre-processing steps (truncation of wavenumber range, normalization, and derivitization). A direct comparison of α-helix to β-sheet ratios calculated by these two programs was done and individual cluster results within a program and individual spectral ratios were compared to cluster ratios. As a result it was determined that clustering results in a "smoothing" effect of the spectra. There was little, if any, consistency leaving extreme doubt in the results. After all, wheat is a plant material and nature typically results in heterogeneity.

Previously Described Secondary Structure Analysis Methods

Reversion back to individually processing data led to further consideration of reducing the analysis time. Various methods have been cited to determine protein secondary structure. Piot (A2) performed a process similar to that used in Chapter 1. He used the second derivative to indicate peak position, curve fitting using the sum of Lorentzian and Gaussian functions on baseline corrected, normalized spectra. From this model he measured the area of the α-helix to β-sheet ratios at Raman frequencies 1656 cm^{-1} and 1669 cm^{-1}, respectively. Kniepp et al (A3) used Opus 3.01 software (Bruker Optics, Billeries, MA) to perform second derivative on Savitsky-Golay smoothed spectra. Spectra were vector normalized over 1700-1500cm^{-1}, and the ratio of intensities at 1637 cm^{-1} and 1657 cm^{-1} were measured. In an earlier publication, Kniepp et al. (A4) used Opus 3.0 software. The spectra were tested for absorption of water vapor using peak intensities at 1792.4 cm^{-1} and 1844.6 cm^{-1} as criteria. Intensities, based on second derivative, greater than 2×10^{-5} and 3×10^{-5} were not included in the data evaluation. Offset-corrected, first derivative absorbance spectra whose integral intensities between 1770 cm^{-1} and 1100 cm^{-1} that were higher than 250 and lower than 30 were also excluded. Those spectra that passed these tests were used in PCA and cluster analysis. Ten spectra within the center of each class were averaged together, and the second derivative of these averages were normalized and smoothed with Savitsky-Golay algorithm. Kretlow et al. (A5) recorded the intensities of baseline corrected original absorbance data at peak positions 1637 cm^{-1} and 1657 cm^{-1}. A peak shift was apparent in some spectra from 1657 to 1650 cm^{-1} with decreased alpha helix. After performing second derivative an additional peak at 1625 cm^{-1} appeared and a small downshift from 1655 to 1653 cm^{-1} was observed in some spectra. Lasch et al. (A6) performed a second derivative with a Savitsky-Golay 9-point smooth. Spectra were vector normalized over 2800-

2985 cm^{-1}, an average of three adjacent points was taken and spectral information was removed in specific regions. Other procedures have involved visual inspection (A7), quantification of second derivative intensities (A8), and the use of PROTA database with algorithms developed by outside companies (A9).

A mass email and sample spectra were sent to the authors of these papers in attempts of forming a round robin to achieve an optimal analysis method.

Attempts at Other Methods

Attempts were made at the analysis method offered by Kretlow. The ratio of the peak intensities at 1657 and 1637 cm^{-1} were calculated from a baseline of 1715-1480 cm^{-1}. Initially it seemed that the method worked well. Values were nearly identical to those found in the previously used analysis method **(1)**. The method however, did not work on all wheat data in that oftentimes the values were outside of the predicted hard wheat ratio range of approximately 1.10 to 2.50. Since multiple peaks can add together, it was believed that this method should not be used on native proteins. If, however, pure, synthetically derived, or less complex proteins are being analyzed, this method may be more advantageous.

Using the second derivative intensities to look at secondary structure data resulted in absurd ratios sometimes above 20.

The method used in Chapter 1 was tested with the exact same parameters, in an updated version of GRAMS, AI 7.02 (Thermo Galactic, Thermo Scientific, Waltham, MA). The ratios produced by these methods were different from those using the earlier version.

An extended telephone conversation between Wetzel and Galactic Industries former software writer responsible for two different versions of GRAMS, but not RAZOR, did not resolve the fact that differing versions produced different results even when using the same parameters.

Each successive software product employs its own programmed guidance criteria for the iterative process used. Each is presumed by its author to offer some advantage. Thus selection of one version for comparing spectra regarding secondary structure within a given experimental group (crop year) is necessary for meaningful ranking.

Alterations to Final Method

Since nearly half of the hard wheat data had been processed using the previously described method, there was no need to change horses in the middle of the stream. Alpha-helix to β-sheet ratios from individual spectra resulting in values above 2.50 or below 0.80 were excluded from calculated averages. If the β-sheet peak was extremely low and a peak at 1620 cm^{-1} appeared, the peak at 1620 cm^{-1} was deleted to increase the size of the β-sheet peak. **Figure A.1** is an example of how initially the β-sheet peak is very low resulting in an α-helix to β-sheet ratio of an unrealistic 2.35. After the deletion of the peak at 1620 cm^{-1} the ratio decreases to 1.91. If the α-helix peak appeared closer to 1645 cm^{-1} instead of 1650 cm^{-1} the peak at 1645 cm^{-1} was considered to be the α-helix peak **(Figure A.2)**. Finally, if the α-helix peak was very low, resulting in a ratio of less than 1.00, a peak of a higher frequency such as 1670 cm^{-1} was deleted to increase the size of the alpha-helix peak. **Figure A.3** shows an example of how the α-helix to β-sheet ratio was less than 1.00, but after the deletion of the peak at 1670 cm^{-1}, ratio was a realistic value.

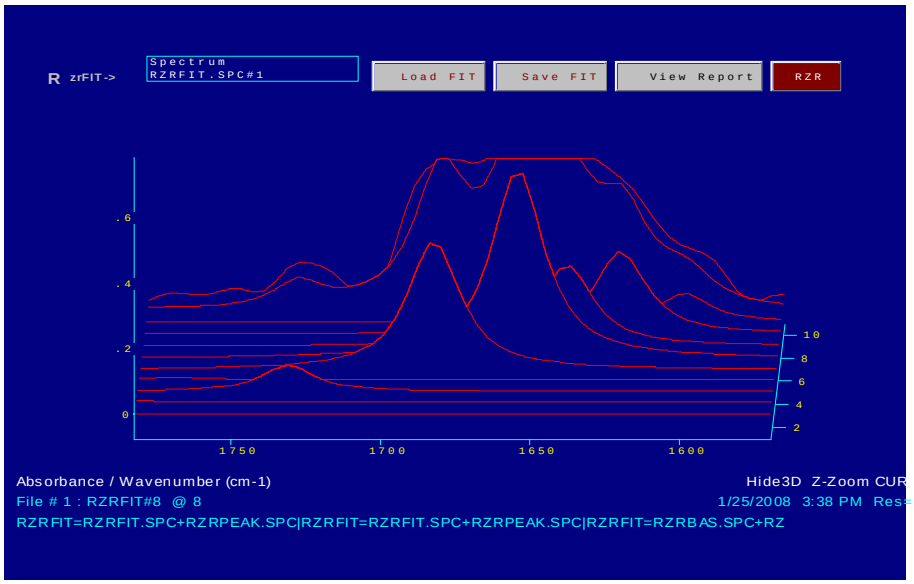

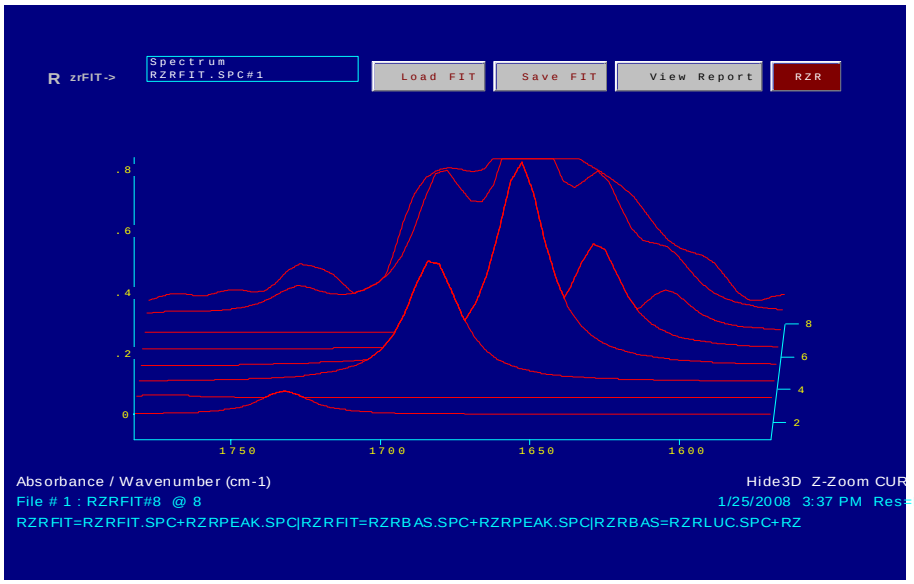

Figure A.1: Protein secondary structure model showing a very small β-sheet peak with an additional peak at 1620 cm^{-1} (top). After deletion of the peak at 1620 cm^{-1}, the β-sheet peak at approximately 1635 cm^{-1} increases.

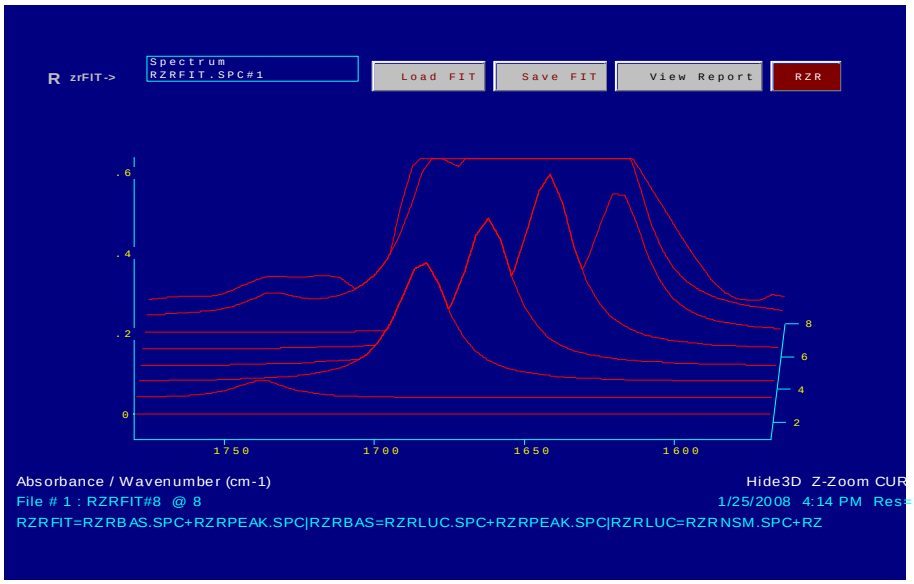

Figure A.2: Protein secondary structure model showing an α-helix peak near 1645 cm^{-1}.

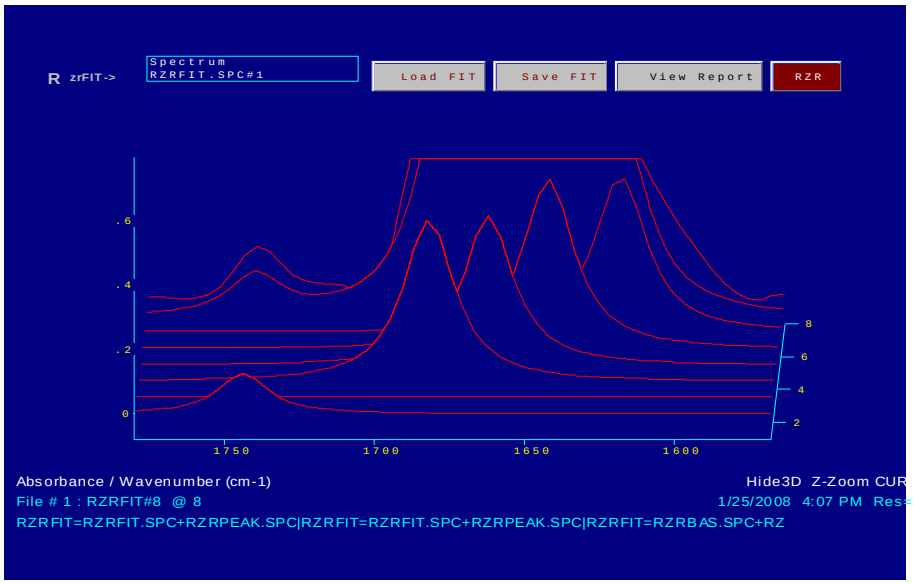

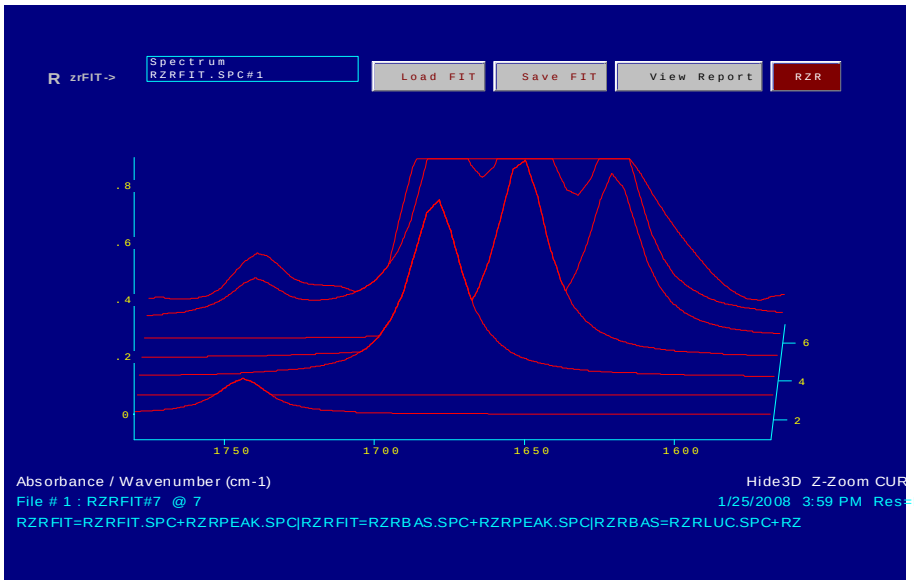

Figure A.3: Protein secondary structure model showing an α-helix to β-sheet ratio of less than 1.00 (top). After the deletion of the peak at 1670 cm^{-1} the ratio increased to approximately 1.22.

Appendix B- Software for Protein Film Data

For all protein film data, it was decided to use the more recent version of the GRAMS software, GRAMS AI 7.02. In this version of GRAMS various parameters need to be manipulated to achieve an optimal model. It was decided to stick with the same region as used in the previous method **(A1)**, 1782-1570 cm^{-1}. This was the amide I region, and there was no need to change this parameter. Spectra recorded from film data had very smooth baselines, therefore it was decided to bypass baseline correction.

Values were calculated using Savitsky-Golay smoothing with various points: 5, 7, 9, and 11. When peak fitting was performed on these spectra, it showed that as the number of smoothing points increased, the fewer peaks were apparent in the curve fit model. All spectra taken from film data were smooth initially; therefore, no further smoothing routine was performed.

Applying a second derivative requires selection of the degree and the number of points. The second and third degree results were visually identical. As the number of points in increased, the amount of smoothing increases. It was decided to stick with the 2^{nd} degree with seven smoothing points to avoid smoothing over peaks.

Attempts were made to skip the deconvolution step and go directly to curve fitting. Results from this were unusual in that location of the α-helix and β-sheet peaks did not correspond to second derivative peaks. For example, instead of the typical 1655 and 1635 cm^{-1} found in the second derivative routine, peaks were found at 1660 and 1640 cm^{-1}.

In the deconvolution step the most important parameter to set is the gamma (γ) factor. The γ factor is related to the full width at half height. The multiply cited paper by Byler and Susi **(A10)**, a full width at half height of 13 was determined to be ideal for protein secondary structure determination. Initial attempts were made with a γ factor of 6.5. A later article by the same authors used a γ factor of 7.5 **(A11)**. Increasing the γ factor, enhances the visible curve formation in deconvolved spectra. It is critical to not over-deconvolve and not eliminate peaks that are present in the spectrum. A smoothing option available within the deconvolution step was not used for reasons described above.

The curve fitting step presented itself with the choice of various parameters. The first is the type of baseline. A linear function is the default, but when the fitting iterations are performed, the baseline is oftentimes shifted to a diagonal. For this reason, an offset baseline was selected, because it resulted in a straight baseline. A Gaussian plus Lorentzian function was used based on previous data analysis articles **(A1, A6)**. The full width at half height of 13 was selected. Finally a low sensitivity was used. The higher the sensitivity, the more peaks there are to deal with. Fifty iterations were adequate for curve fitting. If after the 50 iterations were performed, a peak was shown as having a negative area, those peaks were deleted and 50 additional iterations were performed.

After curve fitting was complete, the location of the model peaks was checked with the location of the peaks in the second derivative. A few times, a peak that was in the second derivative was not in the curve fit model. If this was the case, a peak was added in the model, before the 50 iterations of fitting.

In conclusion, for any protein secondary structure analysis method that is used, it is important to stick with one software program. Each program, even newer versions of the same could give slightly different results. For comparison and ranking of data, it is critical to stick with the same program. Although deconvolution and curve fitting are subjective, as long as the second derivative spectra match with the peaks seen in the deconvolved and curve fit model, it is probably reliable.

References Cited in Appendices A and B

A1. Wetzel, D.L., Srivarin, R. and Finney, J.R. 2003. Revealing protein infrared spectral detail in a heterogeneous matrix dominated by starch. *Vib. Spectros.* 31, 109-114.

A2. Piot, O., Autran, J.-C. and Manfait, M. 2000. Spatial distribution of protein and phenolic constituents in wheat grain as probed by confocal Raman microspectroscopy. *J. Cereal Sci.* 32:57-71.

A3. Kniepp, J., Miller, L.M., Jonsis, M., Kittel, M., Lasch, P., Beekes, M., and Naumann, D. 2003. In situ identification of protein structural changes in prion-infected tissue. *Biochimica et Biophysica Acta (BBA) - Molecular Basis of Disease***.** 1639(3): 152-158.

A4. Kniepp, J., Lasch, P., Baldauf, E., Beeked, M., and Naumann, D. 2000. Detection of pathological molecular alterations in scrapie-infected hamster brain by Fourier transform infrared (FT-IR) spectroscopy. *Biochimica et Biophysica Acta (BBA) - Molecular Basis of Disease.* 1501(2-3) 189-199.

A5. Kretlow, A, Wang, Q., Kneipp, J., Lasch, P., Beekes, M., Miller, L., and Naumann, D. 2006. FTIR-microspectroscopy of prion-infected nervous tissue. *Biochimica et Biophysica Acta (BBA) - Biomembranes*. 1758(7): 948-959.

A6. Lasch, P., Schmitt, J., Beekes, M., Udelhoven, T., Eiden, M., Fabian, H., Petrich, W., and Naumann, D. 2003. Antemortem identification of bovine spongiform encephalopathy from serum using infrared spectroscopy. *Anal. Chem.* 75(23): 6673-6678.

A7. Miklossy, J., Kis, A., Radenovis, A., Miller, L., Forro, L., Martins, R., Reiss, K., Darbinian, N., Darekar, P., Mihaly, L., and Khalili, K. 2006. Beta-amyloid and Alzheimer's type changes induced by Borrelia spirochetes. *Neurobiology of Aging*. 27: 228-236.

A8. Dong, A., Huang, P., and Caughey, W.S. 1990. Protein secondary structures in water from second-derivative amide I infrared spectra. *Biochemistry.* 29(13):3303-8.

A9. Shah, P.S., Bizik, F., Dukor, R.K., and Qasba, P.K. 2000. Active site studies of bovine α1→3-galactosyltransferase and its secondary structure prediction. *Biochimica et Biophysica Acta (BBA) - Protein Structure and Molecular Enzymology*. 1480(1-2): 222-234.

A10. Byler, D.M., and Susi, H. 1986, Examination of the Secondary structure of proteins by deconvolved FTIR spectra. *Biopolymers*, 25, 469-487.

A11. Yang, W.J., Griffiths, P.R., Byler, D.M., and Susi, H. 1985. Protein conformation by infrared spectroscopy resolution enhancement by Fourier self-deconvolution. *Appl. Spectros.* 39 (2), 282-287.